Modeling investigations on gas permeameters: spatial weighting functions and layered systems

By:
Eric C. Aronson

Submitted in Partial Fulfillment of the Requirements
for the Degree of Master of Science in Hydrology

New Mexico Institute of Mining and Technology
Department of Earth and Environmental Sciences
Socorro, New Mexico
May, 1999

Abstract

Modeling investigations on gas permeameters:
spatial weighting functions and layered systems
by:
Eric C. Aronson

Two very different investigations are brought together in this work. These share the common approach of numerical investigation through the finite element method, and both involve gas minipermeameters. Minipermeameters are instruments which measure permeability by injecting gas into a sample, and monitoring the applied pressure and flow rate. The first investigation, Determination of Spatial Weighting Functions Using Adjoint State Sensitivity Analysis, stresses both the introduction of a new theoretical technique and the illustration of the technique on the minipermeameter. The second investigation, Determination of Geometric Factors for a Layered Permeability System, lays a foundation for the expansion of practical uses of the permeameter by introducing new geometric factors for layered permeability systems.

When an instrument makes a measurement, an effective property is inverted that may be viewed as a spatial average of the properties of the materials which compose the total volume sampled. Therefore it is important to understand the extent of that volume, and the relative importance of different regions within the volume. Linear filter theory suggests that we may view effective permeability as the convolution of point scale permeability and a spatial weighting function over the volume of the sampled rock. The weighting functions, which are isolated by employing adjoint state sensitivity analysis, describe the importance of the local permeability at the point scale to the effective permeability yielded by the minipermeameter.

After developing the theoretical technique, the finite element method was employed to determine the linear spatial weighting functions for the minipermeameter. Since an extremely fine discretization level was used, the field of point scale weighting functions were also estimated. The weighting functions indicate that the region directly beneath the tipseal no-flow boundary makes the greatest contribution to the measurement. Integrating the weights over a volume indicated that 95% and 99% of the weighting function is contained in a right cylinder with dimensionless radius and length of 2.3, and 3.71, repectively. These values are in good agreement with the numerical and experimental observations of several previous investigators. Additionally, it was found that the spatial weighting functions are in near perfect correlation with an equation relating the potential gradient and the geometric factor.

Chapter 3 presents the investigation to determine new geometric factors for a layered permeability system. This should prove useful for investigating the permeability across narrow faults. Currently, measuring permeability in narrow deformation bands typically results in a permeability measurement that is an average of the deformation

zone and host rock permeability. This work develops the basis for expanding field permeametry so that the permeability of one of two layers may be measured when independent measurement of the other layer permeability and the thickness of the upper layer is available.

The geometric factors were determined for the semi-infinite flow geometry and a tipseal with ratio (b_d) of 2. Used in the traditional form of the minipermeameter equation, 133 values of the two layer geometric factors were found to also be a function of the dimensionless thickness of the upper layer (D), and the ratio of the layer permeabilities (K_R). As a function of K_R for a particular D, the geometric factor curve is characterized by two asymptotes and a smooth transition zone. Regressions were performed to determine equations which accurately (within 6.5%) characterize the curve for all values. Using either the data sets, or the regression curves and the two layer permeameter equation, a unique value of permeability may be quickly determined either graphically or using a non-linear search

Acknowledgements

I would also like to acknowledge my committee members: Dr. John L. Wilson, Dr. Brian McPherson, and Dr. Jan Hendrixx. Thanks Brian, for the early-on, healthy exchange of ideas. A special thanks to Dr. Wilson for providing a research assistantship and many opportunities to be involved in projects outside of, and tangent to this work, as well as the broad range of advice as my primary advisor. It was Dr. Wilson who suggested using the adjoint method as an approach to computing spatial weighting functions.

The time at New Mexico Tech has been a great opportunity for personal and professional growth, due to many fine people. In particular, I would like to thank: Robert Holt, who's advice, enthusiasm, and understanding of balance often made this a smoother period of time, and Roseanna Neupaeur for her company and many thoughtful discussions in the 3rd floor computer lab.

Table of Contents

List of Tables

List of Figures

Nomenclature

units: M - mass, L - length, t - time, T - temperature, *mol* - moles, [-] - dimensionless

General

a inner tipseal radius, [L]

b outer tipseal radius, [L]

b_d ratio of tipseal radii, equal to $\dfrac{b}{a}$ [-]

k_{eff} effective intrinsic permeability, [L²]

$G_o(b_d)$ Goggin's geometric factor for the semi-infinite medium, [-]

$G_o(b_d, R_D, Z_D)$ Goggin's geometric factor for the finite medium, bounded by

         dimensionless core radius, R_D, and dimensionless core

         length, Z_D, [-]

M molecular mass of gas [M *mol* $^{-1}$]

$\dot{m}$ mass flow rate into the sample, [Mt^{-1}]

P gas pressure, [ML^{-1}t^{-2}]

P_i pressure inside the tipseal chamber, [ML^{-1}t^{-2}]

P_o ambient pressure outside the tipseal, [ML^{-1}t^{-2}]

Q volumetric flow rate into the sample, [L^{3}t^{-1}]

r radial coordinate, [L]

r_d dimensionless radial coordinate, equal to $\dfrac{b}{a}$ [-]

R gas constant [ML^{-2}T^{-1}t^{-2}*mol* $^{-1}$]

R_D dimensionless core radius, equal to $\dfrac{r}{a}$ [-]

μ gas viscosity, $[Mt^{-1}L^{-1}]$

Φ pseudo-potential, equal to $\dfrac{M}{RT\mu}\dfrac{P^2}{2}$ $[Mt^{-1}L^{-3}]$

Φ_i applied pseudo-potential beneath the tipseal,

$$\text{equal to } \dfrac{M}{RT\mu}\dfrac{P_i^2}{2} \ [Mt^{-1}L^{-3}]$$

Φ_o the "ambient" pseudo-potential outside of tipseal,

$$\text{equal to } \dfrac{M}{RT\mu}\dfrac{P_o^2}{2} \ [Mt^{-1}L^{-3}]$$

z coordinate along axis of symmetry, [L]

z_d dimensionless coordinate along axis of symmetry, equal to $\dfrac{z}{a}$ [-]

Z_D dimensionless core length, equal to $\dfrac{z}{a}$ [-]

Chapter 2 - Adjoint state sensitivity analyses for spatial weighting functions

$\underline{\underline{A}}$ coefficient matrix

$\underline{f}$ general load vector which includes sources/sinks and boundary

   conditions

k permeability of material in a homogeneous system, $[L^2]$

k_j permeability of the jth material in a heterogeneous system, $[L^2]$

$\underline{\dot{m}}$ vector of nodal mass flows, [Mt^{-1}]

N number of volumes comprising V, [-]

J general performance measure

V total volume of sample, [L^3]

$\underline{\alpha}$ general vector of parameter values

$\beta(r,z,\theta)$ spatial weighting functions in cylindrical coordinates [L^{-3}]

$\overline{\beta_j}$ volumetric weighting function for the jth volume [-]

$\underline{\Phi}$ vector of pseudo-potentials at node points

$\underline{\psi}$ vector of partial derivatives of state variables with respect to the jth

   parameter, equal to $\dfrac{\partial \underline{\Phi}}{\partial \alpha_j}$

$\underline{\psi}^*$ vector of adjoint states

Chapter 3 - Two layer permeability geometric factors

A_{lower} fitting parameter that describes the lower asymptote of two-layer

   geometric factor curves, [-]

A_{upper} fitting parameter that describes the upper asymptote of two-layer

   geometric factor curves, [-]

B_1 fitting parameter for two-layer geometric curves, [-]

B_2 fitting parameter for two-layer geometric curves, [-]

d depth to top of lower permeability material, [L]

D dimensionless depth to top of lower permeability layer, equal to $\dfrac{d}{a}$ [-]

$G_D(b_d)$ Geometric factor for the semi-infinite, layered permeability system, [-]

k_T permeability of top layer in a layered permeability system, $[L^2]$

k_B permeability of lower layer in a layered permeability system, $[L^2]$

K_R ratio of upper layer permeability to lower layer permeability,

   equal to $\dfrac{k_T}{k_B}$ [-]

1. Introduction

Two very different investigations are brought together in this work. These share the common approach of numerical investigation through the finite element method, and both involve gas minipermeameters. Minipermeameters are instruments which measure permeability by injecting gas into a sample, and monitoring the applied pressure and flow rate (Eijpe and Weber, 1971; Goggin et al., 1988; Davis et al., 1994; Suboor and Heller, 1995; Tidwell and Wilson, 1997). The first investigation, *Determination of Spatial Weighting Functions Using Adjoint State Sensitivity Analysis*, stresses both the introduction of a new theoretical technique and the illustration of the technique on the minipermeameter. The second investigation, *Determination of Geometric Factors for a Layered Permeability System*, lays a foundation for the expansion of practical uses of the permeameter by introducing new geometric factors for layered permeability systems.

Since it is recognized that the reader may not be interested in both investigations, this work has been divided to allow the reader to locate the material that they may be interested in, while avoiding the redundancy of having two stand alone investigations. The reader interested in the newly proposed technique to determine spatial weighting functions, would probably be interested in the balance of this chapter and all of Chapter 2. The reader wishing to use a minipermeameter to measure permeability in layered systems could look here and in Chapter 3. The reader with a general interest in permeametry may find all chapters to be of interest.

This introductory chapter gives a brief overview of the background common to both investigations: permeameters and the finite element code. Chapter 2 discusses a newly proposed technique of using adjoint state sensitivity analyses to determine linear spatial weighting functions and the application of this technique to the minipermeameter. Linear filter theory (Matheron, 1965; Marle, 1967; Baveye and Sposito, 1984; Cushman, 1984; Desbarats, 1992) suggests that we may view effective permeability as the convolution of point scale permeability and a spatial weighting function over the volume of the sampled rock. The weighting functions, which are isolated by employing adjoint state sensitivity analysis, describe the importance of the local permeability at the point scale to the effective permeability yielded by the minipermeameter. This chapter also compares this new theory with the results of previous minipermeameter investigations. Chapter 3 presents the investigation to determine new geometric factors for a layered permeability system. This work develops the basis for expanding field permeametry to measure the permeability of one of two layers when independent measurement of the other layer permeability and the thickness of the upper layer is available. A summary of conclusions from both investigations and recommendations for future work are given in Chapter 4.

The balance of this chapter begins with an overview of the development and operation of the gas minipermeameter, and introduces several permeameter studies which relate to the work contained within this paper. It also discusses how boundary conditions were addressed in these investigations. This is followed by a section that outlines the development of the finite element code that was utilized to solve the flow equations for the permeameter. This section is restricted to the equations pertaining to the flow

problem; the extension of the code to solve the adjoint state problem is discussed in

Chapter 2.

1.1 Permeameters

1.1.1 General

Gas permeameters are instruments which measure permeability through steady injection of

a gas into a sample (Eijpe and Weber, 1971; Goggin et al., 1988; Davis et al., 1994;

Suboor and Heller, 1995; Tidwell and Wilson, 1997). The pressure drop through the

material and the flow rate into the sample are used to invert a permeability value. Figure

1.1 is a schematic cross-section through a permeameter tipseal. The tipseal is applied to

the sample face, and an elevated pressure within the internal chamber induces flow into the

sample. The gas flows into the sample and then exits through the free surface beyond the

outer edge of the tipseal. A conformable material, such as silicone rubber, forms a seal

along the sample surface. Tidwell and Wilson (1997) introduced tipseal guides to limit the

deformation of the conformable tipseal, so that the inner and outer radius (a and b,

respectively) remain unchanged.

Development of gas permeametry has advanced slowly over the last half-century. Suboor

and Heller (1995) suggest that the first recorded use of the permeameter was in 1950, by

Dykstra and Parsons (1950). Early permeameters relied on calibration curves to

determine permeability values, which required instrument calibration be performed for the

entire range of possible permeabilities. In 1988, Goggin et al. (1988) presented a formula
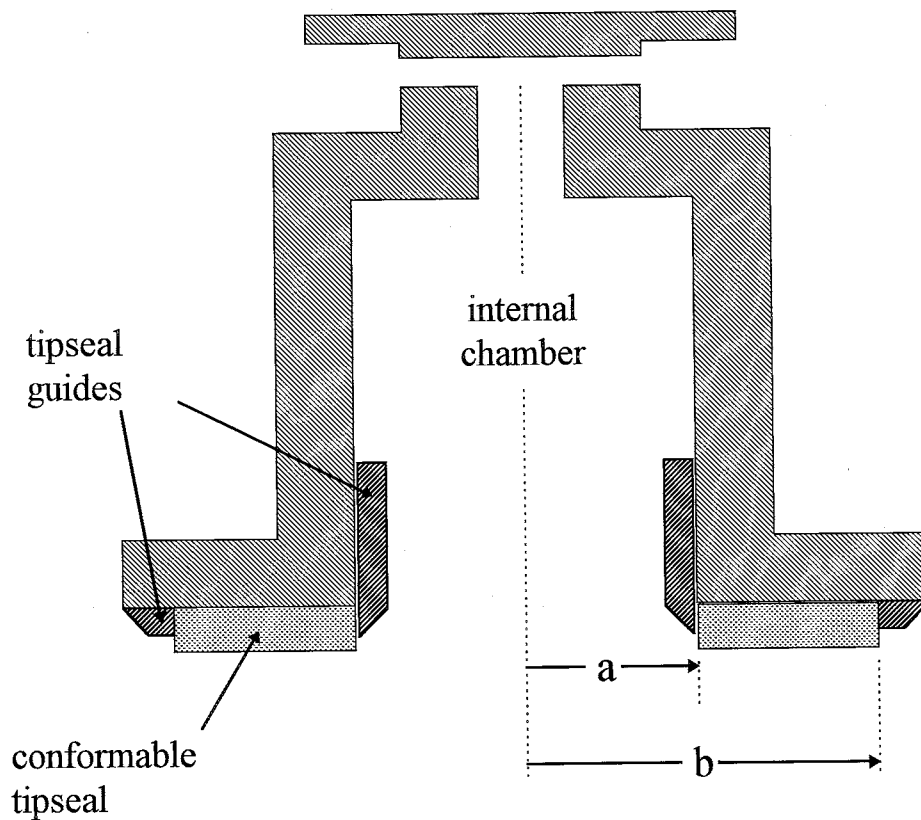
Figure 1.1 - Schematic of minipermeameter tipseal

relating pressures flow rate, tipseal geometry, and sample permeability. Presented as a

modified form of Darcy's law, the formula (1.1) includes a geometric factor that is a

function of the ratio of the outer tipseal radius to inner tipseal radius, and sample

geometry. Although the formula presented by Goggin et al. (1988) is widely used, some

investigators still use calibration curves. For a thorough history of gas permeameter

development, the reader is directed to Suboor and Heller (1995).

$$(1.1) \qquad k_{eff} = \frac{Q \mu P_i}{a G_o(b_d, R_D, Z_D) \dfrac{P_i^2 - P_o^2}{2}}$$

where k_{eff} $\equiv$ effective intrinsic permeability [L^2]

Q $\equiv$ volumetric flow rate into the sample [L^{3}t^{-1}]

P_i $\equiv$ pressure inside the tipseal chamber [ML^{-1}t^{-2}]

P_o $\equiv$ ambient pressure outside the tipseal [ML^{-1}t^{-2}]

μ $\equiv$ gas dynamic viscosity [Mt^{-1}L^{-1}]

a $\equiv$ inner tipseal radius [L]

b $\equiv$ outer tipseal radius [L]

$G_o(b_d, R_D, Z_D)$ $\equiv$ Goggin's geometric factor

b_d $\equiv$ permeameter tipseal ratio, $= \dfrac{b}{a}$

R_D $\equiv$ dimensionless sample radius, $= \dfrac{\text{sample radius}}{a}$

Z_D $\equiv$ dimensionless sample length, $= \dfrac{\text{sample length}}{a}$

Assuming a homogeneous isotropic material, Goggin et al. (1988) determined geometric factors (henceforth called Goggin factors) for two geometries: flow into cylinders with adjacent sides and bottom at finite distances, $G_o(b_d, R_D, Z_D)$, and flow into a semi-infinite halfspace, $G_o(b_d, \infty, \infty)$ or $G_o(b_d)$. A finite difference model was used to determine Goggin factors when sample boundaries (assumed to be constant pressure surfaces) were located at finite distances, and an analytical solution for a ring source was used to estimate

Goggin factors for the semi-infinite geometry. Recently new exact analytical solutions have been derived (B. Kerr and J. Wilson, personal communication, 1998), but they have not yet been published.

1.1.2 Equation development

In the absence of gas slippage effects, the mass conservation equation for radially symmetric, laminar, steady flow of a compressible fluid in cylindrical coordinates (r,z) is:

$$(1.2) \qquad \frac{1}{r}\frac{\partial}{\partial r}\left(rk_r\frac{\rho}{\mu}\frac{\partial P}{\partial r}\right)+\frac{\partial}{\partial z}\left(k_z\frac{\rho}{\mu}\frac{\partial P}{\partial z}\right)=0$$

where $\quad \rho \quad \equiv \quad$ gas density $[ML^{-3}]$

(1.2) is a non-linear equation since the fluid density is a function of pressure. Using the same approach as Goggin et al. (1988), we may produce an identity (1.3) by combining the ideal gas law with a Kirchoff transform. Since viscosity varies little with pressure (but significantly with temperature), the resulting equation (1.4) is essentially linear for isothermal conditions.

$$(1.3) \qquad \rho\frac{\partial P}{\partial x_i}=\frac{M}{2RT}\frac{\partial P^2}{\partial x_i} \quad \text{for } x_i = r,z$$

$$(1.4) \qquad \frac{1}{r}\frac{\partial}{\partial r}\left(rk_r\frac{M}{2\mu RT}\frac{\partial P^2}{\partial r}\right)+\frac{\partial}{\partial z}\left(k_z\frac{M}{2\mu RT}\frac{\partial P^2}{\partial z}\right)=0$$

where   R $\equiv$ gas constant $[M\ L^{-2}\ T^{-1}\ t^{-2}\ mol^{-1}]$

       T $\equiv$ absolute temperature $[T^{-1}]$

       M $\equiv$ molecular mass of gas $[M\ mol^{-1}]$

To further simplify the approach, a pseudo-potential, Φ, is introduced. This results in the form of the differential equation (1.5) that is solved numerically. It is important to note that ideal gas compressibility has been assumed, and that gas slippage effects have not been taken explicitly into account. These effects were not accounted for in the original derivation of Goggin factors, but corrections for these effects are proposed by Goggin et al. (1988). It is readily observed that (1.5) now resembles the standard form of the governing equation for axisymmetric incompressible (eg, liquid) flow.

$$(1.5) \qquad \frac{1}{r}\frac{\partial}{\partial r}\left(rk_r\frac{\partial\Phi}{\partial r}\right)+\frac{\partial}{\partial z}\left(k_z\frac{\partial\Phi}{\partial z}\right)=0$$

$$(1.6) \qquad \text{where } \Phi=\frac{M}{RT\mu}\frac{P^2}{2}\quad [M\ t^{-1}L^{-3}]$$

In this system, the expression for the Darcy velocity, $\underline{u}$, is given by (1.7), where $\underline{\underline{k}}$ is a tensor with diagonal components k_r, k_z.

$$(1.7) \qquad \underline{u} = -\underline{\underline{k}} \frac{1}{\rho} \nabla \Phi = -\frac{k_r}{\rho} \frac{\partial \Phi}{\partial r} \hat{r} - \frac{k_z}{\rho} \frac{\partial \Phi}{\partial z} \hat{z}$$

where $\quad \underline{u} \quad \equiv$ Darcy velocity [L T^{-1}]

The mass flux, $\underline{q}$, is given by

$$(1.8) \qquad \underline{q} = -\underline{\underline{k}} \nabla \Phi = \rho \underline{u} = -k_r \frac{\partial \Phi}{\partial r} \hat{r} - k_z \frac{\partial \Phi}{\partial z} \hat{z}$$

where $\quad \underline{q} \quad \equiv$ mass flux [M T^{-1} L^{-2}]

In terms of our transformed variables, the effective property formula (1.1) becomes

$$(1.9) \qquad k_{\mathit{eff}} = \frac{\dot{m}}{aG_o(b_d)[\Phi_i - \Phi_o]}$$

where $\quad \dot{m} \quad \equiv$ mass flow rate into the sample [M t^{-1}]

$\Phi_i \quad \equiv$ applied pseudo-potential beneath

the tipseal [M t^{-1}L^{-3}]

$\Phi_o \quad \equiv$ "ambient" pseudo-potential [M t^{-1}L^{-3}]

It is also useful to discuss the minipermeameter potential field and other results in terms of dimensionless units, with the inner tipseal as the characteristic length.

$$(1.10) \qquad r_d = \frac{r}{a}$$

$$(1.11) \qquad z_d = \frac{z}{a}$$

$$(1.12) \qquad \Phi_d = \frac{\Phi - \Phi_o}{\Phi_i - \Phi_o}$$

In these dimensionless units, the transformed governing equation, (1.5) becomes:

$$(1.13) \qquad \frac{1}{r_d} \frac{\partial}{\partial r_d} \left(r_d k_r \frac{\partial \Phi_d}{\partial r_d} \right) + \frac{\partial}{\partial z_d} \left(k_z \frac{\partial \Phi_d}{\partial z_d} \right) = 0$$

1.1.3 Relevant Permeameter Investigations

Several investigators report studies which attempt to describe the regions that the

permeameter interrogates. An understanding of the results of these studies provides both

a good starting point for addressing the numerical studies at hand, and also provides a

source of comparison for the results of Chapter 2. Goggin et al. (1988) and Chen (1992)

drew conclusions regarding permeametry sampling based on results from studies

employing finite difference methods. Suboor and Heller (1995) utilized the scanning

minipermeameter of the New Mexico Petroleum Recovery Research Center (PRRC) for

empirical investigations regarding permeameter sampling traits. Also of interest

(predominately to the investigation in Chapter 2), is the work of Tidwell and Wilson

(1997) and Tidwell et al. (1999), who have employed an automated scanning

minipermeameter in upscaling studies.

Some insight into permeameter sampling regions is found in the original investigation by Goggin et al. (1988) that resulted in the permeameter equation and values for the geometric factors. By examining differences in geometric factors between the semi-infinite and finite geometries, Goggin et al. concluded that, for samples with dimensionless radius and depth of 4, less than 5% difference in permeability results for a significant range of tipseal ratios.

Using a finite difference model, Chen (1992) proposed a methodology for measuring porosity by monitoring the transient pressure decay after steady-state injection for the semi-infinite sample. To eliminate the dependence on sample boundaries, Chen studied the changes in the Goggin factor for various sample sizes and different "infinite" boundary conditions. Chen also examined the distribution of flow entering and leaving the sample to draw conclusions regarding the importance of the regions sampled.

To determine the value of the semi-infinite geometric factor, Chen (1992) compared simulations where the "infinite" boundaries were either both constant potential or no-flow. He proposed that the correct semi-infinite geometric factor must lie between the geometric factors calculated from these two cases. By increasing the sample size, the range of calculated geometric factors converged to a single value. When $R_D = Z_D = 9$, Chen's geometric factor varied by less than 0.2%. Averaging the values for these two sets of boundary conditions, Chen's semi-infinite geometric factor, $G_o(b_d = 2)$ was 5.22. It is important to note that, for the utilized discretization level, almost 40% of the mass flux entered the sample in the grid block just inside the conformable tipseal, and greater than

35% exited the sample through the first block outside the conformable tipseal. Chen noted this region of concentrated flux and suggested that the portion of the sample contributing to the measurement is predominately in this region.

To address the influence of boundary locations for the permeameter geometry, Chen (1992) held a particular (lateral or depth) boundary location constant at a large distance and then, varying the other boundary location, he compared geometric factors for different "infinite" boundary conditions. Chen observed that for $R_D = 4.0$ ($Z_D = 7.0 \approx \infty$), the error in the geometric factor from the constant potential simulations was only 0.8% and the error for the no-flow simulation was 3.0 %. Further illustrating the effect of the boundary condition type on the geometric factor, Chen showed that samples characterized by dimensionless lengths $R_D = Z_D = 2.5$, deviated from the "exact" geometric factor by 5.8% for the constant potential "infinite" boundaries, and 17.8 % for the no flow boundaries.

An important influence on Chen's (1992) results are the discretization levels that were utilized. He decided on the appropriate finite difference block size by comparing the impacts of round-off and truncation error for the transient solution (in preparation for the porosity problem). Using a one-dimensional flow field and corresponding analytical solution, he found that considerable round-off error was introduced when the grid blocks were smaller than 0.10 (dimensionless with respect to inner radius). This discretization level was then utilized for the axis-symmetric simulations. The effect of Chen's choice of grid block size resulted in calibration to a geometric factor, 5.22, that differs from the

recent analytical semi-infinite value of 5.10 derived by Kerr and Wilson (personal communication, 1998). In the absence of round-off error (steady-state solution with multiple passes to an iterative solver) and with very fine discretization, a similar analysis using the finite element model of this investigation converges to 5.099 ± 0.005, the analytical value.

Suboor and Heller (1995) performed laboratory experiments similar to Chen's numerical investigation, using the scanning minipermeameter of the New Mexico Petroleum Recovery Research Center (PRRC), Berea sandstone, and glass beads. Separate experiments were designed to independently determine the dimensionless radius and depth of investigation. They defined this limiting dimension as the location which would result in a 1% change in measured permeability.

Using a block of Berea sandstone, two sets of measurements were performed to investigate the lateral extent of the region investigated. One set of measurements was made with the adjacent side (at R_D) open to ambient room pressure, and a second set with an impermeable barrier to flow (modeling clay) along the side. They compared the measurement sets to determine the location where measured permeability was impacted by the boundary condition. To determine the depth of investigation, they used a layered system composed of Berea sandstone and glass beads. Repeated measurements were made for different thicknesses of the upper layer Berea sandstone, for which independent permeability measurements were available prior to the reduction in thickness. It is unclear what the lateral and lower boundary conditions were in this part of the investigation.

Using this approach for different tipseal ratios, they determined the depth at which the ratio of the layered-system permeability to the Berea permeability varied by 1%. Suboor and Heller reported their results in terms of dimensionless lengths, determined as the ratio of the location at which a 1% permeability change was observed divided by the outer tipseal radius. Restated in terms of the inner radius (as is the convention throughout this paper), they determined a dimensionless radius of 2.88 and depth of 3.50 for b_d=2.

The approach utilized to determine the horizontal radius of influence is almost the empirical equivalent to the analysis of Goggin et al (1999) and Chen (1992), since it measures the point at which the boundary conditions begin to influence the effective permeability. Since altering the boundary conditions results in a different flow field, it is unclear the extent to which the determined lengths apply to the flow conditions for which the Goggin parameter was developed. In the case of the depth of investigation, our numerical investigations using a two permeability layered system (Chapter 3) show that the depth at which a 1% change results depends on the ratio of the layer permeabilities. In Suboor and Heller's experiment this is the ratio of the Berea sandstone permeability to the glass bead permeability.

Tidwell et al. (1999) employed an automated Multi-Support Permeameter (Tidwell and Wilson, 1997) to obtain large permeability data sets on a relatively homogeneous sample of Berea sandstone. Using four tipseals (all b_d=2), with inner tipseal radius ranging from 0.15 cm to 1.27 cm, they obtained permeability measurements along 0.85 cm grids on each face of the sample. Using the 2304 measurements from a single face of the rock,

they calculated linear spatial weighting functions which relate the permeability

measurements obtained at the different scales. Since the divergent flow geometry of the

permeameter is three dimensional relative to the plane of sampling, these weighting

functions are essentially two-dimensional estimates.

Using the data sets for two tipseals, Tidwell et al. (1999) used a Fourier analyses to

determine linear weighting functions (dependant on each tipseal pair) for both arithmetic

and power averages. The Fourier weighting function may be separated into two real

components, one describing the amplitude change and the other describing the phase shift.

They found that the phase shift was essentially zero, and therefore, the gain function alone

describes the Fourier weighting function. For the power average weighting functions,

they found that employing an ad hoc approach of scaling the gain by the magnitude at zero

frequency, resulted in the same function, regardless of the power average exponent used.

Fitting a model to cross sections of the inverse transformed weighting functions, Tidwell

et al. (1999) found that the weighting function was centered over the measurement (of the

larger tipseal) and decayed as a non-linear function of radial distance. If we assume that

the models fit to the cross-sections (in their Figure 10) represent the average cross-

sections for each tipseal set, then integrating the models over the surface can be used to

estimate the cumulative weight as a function of radius. For the tipseal pair that relates the

permeability measurements at the most disparate scales (1.27-0.15 cm filter),

dimensionless radii of 1.73 and 1.87 contain 90% and 95% of the weighting function,

respectively. It should be noted that the weighting functions arising from their study

represent two-dimensional weighting functions for a specific tipseal pair. Although it was beyond the scope of their paper, the authors recognized that these large data sets could be used to estimate a two-dimensional, point scale spatial weighting function (similar to the three-dimensional spatial weighting function, $\beta(r, z, \theta)$, estimated in Chapter 2).

1.1.4 Flow Geometry for the current investigations

Goggin determined geometric factors for both a semi-infinite geometry (where the sample has no far field boundaries), and for finite samples that are bounded (at some R_D and Z_D) by constant potential boundaries. As Chen illustrated, three more groups of geometric factors also exist: for a finite sample with far-field boundaries that are barriers to flow (possibly required for cores of poorly consolidated rocks, which would be contained in an impervious sleeve), and two groups which have mixed (one no-flow and one constant potential) boundary conditions. As the radius and thickness of the finite sample increase, the geometric factors approach those for the semi-infinite case.

For all of the work presented here, only the semi-infinite geometry was investigated. This decision was based on the need to limit the number of influences on the geometric factor and flow field for both studies. The semi-infinite geometry was judged to be the more general case, since 1) it is often possible to control either the tipseal or sample size so that the semi-infinite geometry is approximated, and 2) field studies where measurements are made in situ are represented by the semi-infinite geometry. To achieve

this numerically, it is necessary to use a domain in which these "infinite boundaries" are

located at distances such that simulation results are not significantly impacted.

$$\frac{\partial \Phi}{\partial z} = 0$$

Φ_1 Φ_o

axis of symmetry

$$\frac{\partial \Phi}{\partial r} = 0$$

either Φ_o

or $\frac{\partial \Phi}{\partial r} = 0$

"semi-infinite" boundaries

either Φ_o or $\frac{\partial \Phi}{\partial z} = 0$
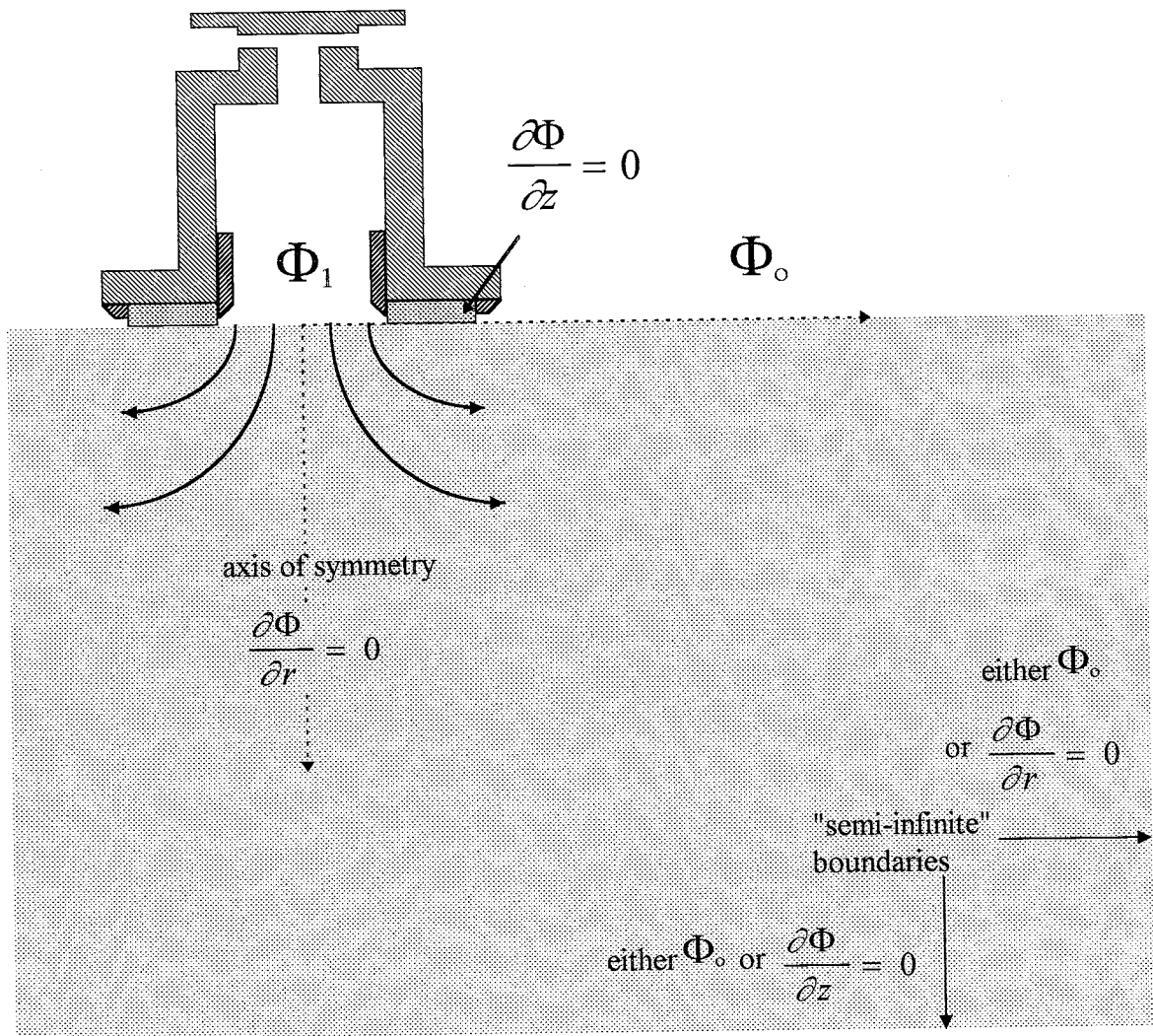
Figure 1.2 - Geomoetry and boundary conditions for the minipermeameter problem.

Figure 1.2 shows a schematic of the geometry and boundary conditions for which the

minipermeameter problem was solved. After the governing equation is linearized (1.5 and

1.6), the constant pressure applied within the tipseal chamber, P_i, and the constant

ambient pressure outside of the sample, P_o, are represented by constant pseudo-potentials

(Φ_i and Φ_o, respectively). The conformable seal is represented by a zero mass flux boundary. Due to the symmetry in the homogeneous flow field, the axis of symmetry is also modeled as a zero mass flux boundary. To determine appropriate distances so that the "semi-infinite" boundaries did not effect results, simulations with different domain sizes were performed where both distant boundaries had either constant potential or no-flow conditions. Appropriate minimum distances were chosen when the Goggin factor resulting from both simulations varied less than 0.1 % from $G_o(b_d) = 5.10$, the analytical solution of Kerr and Wilson (personal communication, 1998).

1.2 Development of the finite element code

Both the state and adjoint problems were solved using the finite element method (Celia and Gray, 1992; Heubner and Thornton, 1982; Wang and Anderson, 1982). For this problem, that of a semi-infinite domain with the predominance of flow concentrated beneath the tipseal, an important advantage of the chosen method is the ease with which finite elements accommodate non-uniform grid spacing. Based on the Galerkin formulation of the method of weighted residuals, equations for triangular elements with linear weighting functions were derived and implemented in a Fortran program. An overview of these processes, as they relate to the state problem, is given in the following section.

1.2.1 Derivation of equations

In the finite element method, the numerically approximated potential ($\widetilde{\Phi}$)[1] within the domain is defined in terms of a linear combination of the *nn* (the number of nodes) nodal potentials($\widetilde{\Phi}_p$), and the nodal basis functions (N_p). The basis functions are used to interpolate the nodal potentials throughout the domain. The nodal potentials are then sought so that this proposed form of the solution (1.14) will satisfy the governing equation.

$$(1.14) \qquad \widetilde{\Phi} = \sum_{p=1}^{nn} N_p \widetilde{\Phi}_p$$

In the method of weighted residuals, the governing solution is first multiplied by weighting functions, and integrated over the volume, V, of the domain. In the Galerkin formulation, these weighting functions are the same as the basis functions. This yields *nn* equations which are used to solve for the *nn* potentials.

$$(1.15) \qquad \int_V \underbrace{\left[\frac{1}{r}\frac{\partial}{\partial r}\left(r k_r \frac{\partial \widetilde{\Phi}}{\partial r} \right) + \frac{\partial}{\partial z}\left(k_z \frac{\partial \widetilde{\Phi}}{\partial z} \right) \right]}_{\text{the weighted residual}} N_p\, dV = 0$$

The system of equations (1.16), which are ultimately derived from (1.15), are then solved to determine the vector of nodal potentials, $\underline{\widetilde{\Phi}}$, which minimizes the sum of the weighted

---

[1] Only used in this section to distinguish the numerically derived potentials from the "true" potentials.

residuals. Each of the nodal potentials, $\tilde{\Phi}_p(r_p, z_p)$, is the numerical approximation to the "true" potential Φ at $(r = r_p, z = z_p)$.

(1.16) $\quad\quad \underline{\underline{A}}\,\tilde{\underline{\Phi}} = \underline{f}$

where $\quad \underline{\underline{A}} \quad \equiv$ coefficient or conductivity matrix

$\quad\quad\quad\quad \underline{f} \quad \equiv$ load vector

$\quad\quad\quad\quad \tilde{\underline{\Phi}} \quad \equiv$ vector of nodal potentials

Using the chain rule and expanding, we may rewrite (1.15) as (1.17). Here, the left most integral pertains to the quantity of substance within the domain, and the other integral is a measure of the substance entering or leaving the domain.

(1.17)
$$\int_V \left[k_r \frac{\partial N_p}{\partial r} \frac{\partial \tilde{\Phi}}{\partial r} + k_z \frac{\partial N_p}{\partial z} \frac{\partial \tilde{\Phi}}{\partial z} \right] dV$$
$$= \int_V \left[\frac{1}{r} \frac{\partial}{\partial r} \left(r N_p k_r \frac{\partial \tilde{\Phi}}{\partial r} \right) + \frac{\partial}{\partial z} \left(N_p k_z \frac{\partial \tilde{\Phi}}{\partial z} \right) \right] dV$$

Applying Green's theorem to the integral on the right side allows us to rewrite the equation (1.18) in terms of the mass flux, $\underline{q}$, entering or leaving the domain through the surface bounding the domain, Γ. This represents the specified flux boundary conditions, and the values are stored in the load vector, $\underline{f}$.

$$(1.18) \qquad \int_V \left[\frac{1}{r} \frac{\partial}{\partial r} \left(r N_p k_r \frac{\partial \tilde{\Phi}}{\partial r} \right) + \frac{\partial}{\partial z} \left(N_p k_z \frac{\partial \tilde{\Phi}}{\partial z} \right) \right] dV = \int_\Gamma N_p \underline{q} \cdot \underline{n} \, d\Gamma$$

$$\text{where} \quad \underline{q} = -k_r \frac{\partial \tilde{\Phi}}{\partial r} \hat{r} - k_r \frac{\partial \tilde{\Phi}}{\partial z} \hat{z}$$

$$\underline{n} \equiv \text{unit normal outward vector on } \Gamma$$

For the first integral in (1.17), two important aspects of the basis functions allow us to quickly assemble the system of nn equations by evaluating element by element, instead of node by node. First, each nodal basis function is defined as zero outside of the patch of elements shared by the node. Secondly, within the area or volume bounded by each element, the nodal basis function is described in terms of the coordinates of the nodes composing that element. Dividing the nodal basis functions into the components that apply to each element, the potential within an element is described in terms of only the element basis functions (N_p^e) and node potentials composing that element. For triangular elements (comprised of nodes i, j and m) with linear basis functions, the potential for the area within an element e is defined as:

$$(1.19) \qquad \tilde{\Phi}^e(r,z) = N_i^e(r,z) \tilde{\Phi}_i + N_j^e(r,z) \tilde{\Phi}_j + N_m^e(r,z) \tilde{\Phi}_m$$

$$\text{where} \qquad N_i^e(r,z) = \frac{1}{2A^e} \left[(r_j z_m - r_m z_j) + (z_j - z_m)r + (r_m - r_j)z \right]$$

$$(1.20) \qquad N_j^e(r,z) = \frac{1}{2A^e} \left[(r_m z_i - r_i z_m) + (z_m - z_i)r + (r_i - r_m)z \right]$$

$$N_m^e(r,z) = \frac{1}{2A^e}\left[(r_i z_j - r_j z_i) + (z_i - z_j)r + (r_j - r_i)z\right]$$

and
$$A^e = \frac{1}{2}\left[r_m(z_i - z_j) + r_i(z_j - z_m) + r_j(z_m - z_i)\right]$$

Differentiating (1.19) and (1.20), substituting into the element form of the differential equation, integrating with respect to the volume of the element (V^e), and rearranging yields (1.21). The rearranged form of (1.21) can be seen to readily resemble the left hand side of (1.16).

$$(1.21) \qquad \int_{V^e}\left[k_r \frac{\partial N_p^e}{\partial r}\frac{\partial \tilde{\Phi}}{\partial r} + k_z \frac{\partial N_p^e}{\partial z}\frac{\partial \tilde{\Phi}}{\partial z}\right]dV^e$$

$$= 2\pi \overline{R}A^e\left\{\left(k_r \frac{\partial N_i^e}{\partial r}\frac{\partial N_L^e}{\partial r} + k_z \frac{\partial N_i^e}{\partial z}\frac{\partial N_L^e}{\partial z}\right)\tilde{\Phi}_i\right.$$

$$+\left(k_r \frac{\partial N_j^e}{\partial r}\frac{\partial N_L^e}{\partial r} + k_z \frac{\partial N_j^e}{\partial z}\frac{\partial N_L^e}{\partial z}\right)\tilde{\Phi}_j \qquad \text{for } L = i,j,m$$

$$\left.+\left(k_r \frac{\partial N_m^e}{\partial r}\frac{\partial N_L^e}{\partial r} + k_z \frac{\partial N_m^e}{\partial z}\frac{\partial N_L^e}{\partial z}\right)\tilde{\Phi}_m\right\}$$

$$\text{where } \overline{R} = \frac{(r_i + r_j + r_m)}{3}$$

By cycling through the elements, the nine contributions (1.22) from each element - denoted by the superscript e, are then added into the appropriate locations in the global conductivity matrix, $\underline{\underline{A}}$, according to the global node numbers of i, j, and m.

$$A^e_{i,L} = 2\pi \overline{R} A^e \left(k_r \frac{\partial N^e_i}{\partial r} \frac{\partial N^e_L}{\partial r} + k_z \frac{\partial N^e_i}{\partial z} \frac{\partial N^e_L}{\partial z} \right) \quad for\ L = i,j,m$$

$$(1.22) \qquad A^e_{j,L} = 2\pi \overline{R} A^e \left(k_r \frac{\partial N^e_j}{\partial r} \frac{\partial N^e_L}{\partial r} + k_z \frac{\partial N^e_j}{\partial z} \frac{\partial N^e_L}{\partial z} \right) \quad for\ L = i,j,m$$

$$A^e_{m,L} = 2\pi \overline{R} A^e \left(k_r \frac{\partial N^e_m}{\partial r} \frac{\partial N^e_L}{\partial r} + k_z \frac{\partial N^e_m}{\partial z} \frac{\partial N^e_L}{\partial z} \right) \quad for\ L = i,j,m$$

1.2.2 Implementation

After derivation of the fundamental equations, a general Fortran program was developed and verified for standard axisymmetric flow problems. Due to the domain size and desired resolution, compact storage was utilized to store the large sparse matrices and an iterative solver was utilized to solve the large system of equations. This significantly reduces the memory required for large simulations (which allows for liberal use of double precision) and greatly decreases the time required for simulation.

The preconditioned conjugate gradient method (Reid, 1971; Young, 1971), as implemented in the subroutine ILUCG (Yeh et al., 1993; Yeh and Srivastava, 1992), was utilized to solve the system of equations (1.16). ILUCG uses an incomplete lower upper preconditioner, and provides relatively quick convergence for large, sparse matrices in compact storage. To guard against round-off error and premature convergence, final convergence was determined by monitoring the Euclidean norm of the residuals. Failure

of the norm to meet a specified tolerance results in an additional pass through the solver using the result from the previous pass as the initial guess.

As is the geometry for which Goggin's geometric factors are derived, the media for all "samples" was assumed isotropic $k_r = k_z$. It is noted that the results of Chapter 2 and Chapter 3 could be easily extended for anisotropy aligned with the coordinate axis by a simple geometric transform.

2. Determination of Weighting Functions Using Adjoint State Sensitivity Analysis

In hydrology, models are used to assist with issues such as the allocation of groundwater, assessing contaminant fate and transport, and evaluating remediation schemes. Models include conceptualizations involving the relationships between and values of spatially distributed properties, which in turn mandate the use (and design) of instruments that measure these properties. In this chapter, a novel approach, which combines adjoint state sensitivity analysis and linear weighting functions, is proposed as a valuable tool to assist in both instrument design and data acquisition.

When an instrument makes a measurement, an effective property is inverted that may be viewed as a spatial average of the properties of the materials which compose the total volume sampled. Therefore it is important to understand the extent of that volume, and the relative importance of different regions within the volume. This knowledge is crucial to assessing the quality of the resulting effective measurement, constraining appropriate application of the acquired data, and design of successful sampling strategies.

The permeameter is an instrument that is utilized to make measurements of intrinsic permeability - the ability of a sample to conduct fluid. Permeameters have been used in a wide variety of investigations, which include examining spatial variability in both

field and laboratory studies (eg., Davis et al., 1990; Dreyer et al., 1990; Suboor and Heller, 1995; Antonellini and Aydin, 1994; Sigda et al., 1999), and permeability upscaling studies (Tidwell and Wilson, 1997; Tidwell et al., 1999). The effective permeability that results from a permeameter measurement is inverted using a formula which includes numerically derived geometric factors (1.1). Since the geometric factors are derived for specific boundary conditions, understanding the region contributing to each measurement is important for appropriate application of the inversion formula. For example, permeability measurements of a porous matrix should be avoided when the region contributing to the effective permeability includes root tubules, fractures, or large sediment grains (relative to the tipseal radius) in high contribution regions. In both spatial variability and upscaling studies, the importance of understanding the regions sampled is particularly amplified since this is fundamental to developing and utilizing the spatially distributed data sets.

The primary purposes of this chapter are 1) introduce the use of adjoint state sensitivity analysis for determining linear spatial filter functions, and 2) demonstrate its application on the minipermeameter. Applying this approach to the minipermeameter yields the relative importance of regions which contribute to the effective permeability. An introduction to and review of the minipermeameter is given in Chapter 1. This chapter continues with reviews of linear filter theory and adjoint state sensitivity analysis which provide the basis for the new approach. This is followed by an overview of the procedure used in the investigation, a discussion of the results, and

finally, conclusions. Included in the final section is a comparison with other approaches used to determine permeameter sampling traits.

2.1 Technique Developement

2.1.1 Weighting functions

Linear filter theory (Matheron, 1965; Marle, 1967; Baveye and Sposito, 1984; Cushman, 1984; Desbarats, 1992) suggests that we may view effective permeability as the integration of the product of point scale permeabilities, k_j, and a spatial weighting function, β, over the volume of the sampled rock (2.1). The weighting function is assumed to integrate to 1. In cylindrical coordinates, this is given by

$$(2.1a) \qquad k_{eff} = \int_V \beta(r,z,\theta)k_j dV$$

$$(2.1b) \qquad 1 = \int_V \beta(r,z,\theta)dV$$

and where k_{eff} ≡ effective intrinsic permeability [L^2]

k_j ≡ point-scale permeability at (r_j,z_j,θ_j) [L^2]

$\beta(r,z,\theta)$ ≡ spatial weighting function [L^{-3}]

V ≡ volume of sample [L^3]

where it has been assumed that the point scale value is isotropic. The weighting functions account for the influence of the measurement process on the effective

measurement (Tidwell et al., 1999). Dividing the rock volume into N smaller volumes, each of which has an essentially homogeneous permeability, we may then define N new weighting functions $(\overline{\beta_j})$ which are derived from integrating the weighting function, $\beta(r, z, \theta)$, over each of the N volumes. For the jth volume, this integrated weighting function is:

(2.2) $\qquad \overline{\beta_j} = \int_{V_j} \beta(r, z, \theta) dV_j$

where $\quad \overline{\beta_j} \quad \equiv \quad$ weighting function for the jth volume [-]

$\qquad V_j \quad \equiv \quad$ the jth volume [L^3]

Then (2.1) may be rewritten as the summation of the product of different weighting functions and the permeability for the smaller volumes (2.3), which in the case of (2.1) is an arithmetic average.

(2.3a) $\qquad k_{eff} = \sum_{j=1}^{N} \overline{\beta_j} k_j$

(2.3b) $\qquad 1 = \sum_{j=1}^{N} \overline{\beta_j}$

A general equation including other non-additive averaging processes can be written (2.4), where $\omega = 1$ gives an arithmetic average, $\omega = -1$ gives a harmonic average, and $\omega = 0$ gives a geometric average.

$$(2.4a) \qquad k_{eff}^{\omega} = \sum_{j=1}^{N} \overline{\beta_j} k_j^{\omega} \qquad \text{for} \qquad \omega \neq 0$$

$$(2.4b) \qquad \ln(k_{eff}) = \sum_{j=1}^{N} \overline{\beta_j} \ln(k_j) \qquad \text{for} \qquad \omega = 0$$

By taking the derivative of both sides of (2.4) with respect to the jth local permeability and rearranging, we may isolate the jth weighting function (2.5). For the arithmetic average, (2.5) reduces to the derivative of the effective permeability with respect to the local permeability (2.6).

$$(2.5a) \qquad \overline{\beta_j} = \frac{dk_{eff}}{dk_j} \left(\frac{k_{eff}}{k_j} \right)^{\omega-1} \qquad \text{for} \qquad \omega \neq 0$$

$$(2.5b) \qquad \overline{\beta_j} = \frac{dk_{eff}}{dk_j} \left(\frac{k_{eff}}{k_j} \right) \qquad \text{for} \qquad \omega = 0$$

To make determinations of the volume of rock sampled and relative importance of regions in the flow field, we assumed a homogeneous material, which is consistent with the development of the Goggin factors for the minipermeameter. Under these conditions, all averaging methods presented reduce to the derivative of the effective

permeability with respect to the local permeability (2.6). Adjoint state sensitivity
analysis is used to determine the derivative.

$$(2.6) \qquad \overline{\beta_j} = \frac{dk_{eff}}{dk_j}$$

2.1.2 Adjoint state sensitivity analysis

Adjoint sensitivity analysis has been used in many fields including electrical
engineering, nuclear reactor assessments, and nonlinear parameter estimation. In
hydrology it has been used for parameter estimation in inverse problems, and to
investigate sensitivities of estimated parameters in numerical models (Sykes et al.,
1985; Sun, 1994). Only a brief overview of equation development is given here, and
the reader is referred to Sykes et al. (1985) or Wilson and Metcalf (1985) for a more
in depth discussion. Here I will follow the general approach presented in Sykes et
al.(1985) which uses Lagrange multipliers.

Applying numerical methods (such as finite difference or finite elements) to the
governing equation (1.5) results in a system of linear equations (1.16 - repeated
below) where $\underline{\underline{A}}$ is the coefficient matrix, $\underline{\Phi}$ is the vector of state values (in our case
the pseudo-potentials) at node points, and $\underline{f}$ is the load vector which includes
sources/sinks and boundary conditions. After $\underline{\underline{A}}$ and $\underline{f}$ are assembled, the system of
equations is solved for the unknown pseudo-potentials.

(1.16) $\underline{\underline{A}}\underline{\Phi} = \underline{f}$

Employment of adjoint state sensitivity analysis yields a vector of first derivatives of a

scalar performance measure with respect to a vector of parameter values. For

example, one may wish to determine the sensitivity of the discharge along a stretch of

river to the distributed recharge values used in model calibration. In this case the

performance measure, J, is the discharge to the river and the parameter list is the

vector of recharge values, $\underline{\alpha}$. Whereas traditional sensitivity analysis would involve

running multiple simulations in which each recharge value was varied, using adjoint

state sensitivity analysis, a single simulation can yield both the state solution and a

vector of sensitivity coefficients, $\dfrac{dJ}{d\underline{\alpha}}$.

(2.7) $\dfrac{dJ}{d\alpha_j} = \dfrac{\partial J}{\partial \alpha_j} + \left[\dfrac{\partial J}{\partial \underline{\Phi}^T}\right]\underline{\psi}_j$

where $\underline{\psi}_j = \dfrac{\partial \underline{\Phi}}{\partial \alpha_j}$ is a vector of partial derivatives of state variables with respect to the

j^{th} parameter. The first term on the right hand side of (2.7) represents the direct

contribution, and the second term represents the indirect contribution.

Taking the derivative of (1.14) with respect to a particular parameter, α_j, and

multiplying the result by a vector of arbitrary constants, $\underline{\psi}^*$, yields (2.8).

$$(2.8) \qquad \underline{\psi}^{*T} \underline{\underline{A}} \underline{\psi}_j + \underline{\psi}^{*T} \left(\frac{\partial \underline{\underline{A}}}{\partial \alpha_j} \underline{\Phi} - \frac{\partial \underline{f}}{\partial \alpha_j} \right) = 0$$

Since (2.8) is identically zero, we may subtract it from (2.7) and rearrange to yield

$$(2.9) \qquad \frac{dJ}{d\alpha_j} = \frac{\partial J}{\partial \alpha_j} - \underline{\psi}^{*T} \left(\frac{\partial \underline{\underline{A}}}{\partial \alpha_j} \underline{\Phi} - \frac{\partial \underline{f}}{\partial \alpha_j} \right)$$
$$+ \underline{\psi}_j{}^T \frac{\partial J}{\partial \underline{\Phi}} - \underline{\psi}_j{}^T \underline{\underline{A}}^T \underline{\psi}^*$$

Since $\underline{\psi}^*$ is a vector of arbitrary constants, we eliminate the need to determine the

vector $\underline{\psi}_j$ for every parameter, by defining $\underline{\psi}^*$ such that

$$(2.10) \qquad \underline{\psi}_j{}^T \frac{\partial J}{\partial \underline{\Phi}} - \underline{\psi}_j{}^T \underline{\underline{A}}^T \underline{\psi}^* = 0$$

(2.10) can be rearranged into the form which is recognized as the adjoint problem

(2.11), and if $\underline{\underline{A}}$ is a symmetric matrix, then the only additional work required for

solution of the adjoint problem is assembling the adjoint load vector, $\dfrac{\partial J}{\partial \underline{\Phi}}$, and solving

the equations.

$$(2.11) \qquad \underline{\underline{A}}^T \underline{\psi}^* = \frac{\partial J}{\partial \underline{\Phi}}$$

The adjoint state, $\underline{\psi}^*$, can be thought of as the change in the performance measure due to a unit injection of mass at that location (Sykes et al., 1985). After solution of (2.11) for the adjoint state vector, equation (2.12), which results from the combination of (2.9) and (2.10), is used to determine the sensitivity coefficients.

$$(2.12) \qquad \frac{dJ}{d\alpha_j} = \frac{\partial J}{\partial \alpha_j} - \underline{\psi}^{*T}\left(\frac{\partial \underline{\underline{A}}}{\partial \alpha_j}\underline{\Phi} - \frac{\partial \underline{f}}{\partial \alpha_j}\right)$$

For the air permeameter investigation, the performance measure is the flow rate of the gas from the instrument into the sample ($\dot{m}$). Using this approach, we can determine the sensitivity of the flow rate (and therefore sensitivity of the effective permeability) to the local permeability associated with a particular location in the flow field:

$$(2.13) \qquad \underline{\underline{A}}^T \underline{\psi}^* = \frac{\partial \dot{m}}{\partial \underline{\Phi}}$$

$$(2.14) \qquad \frac{d\dot{m}}{dk_j} = \frac{\partial \dot{m}}{\partial k_j} - \underline{\psi}^{*T}\left(\frac{\partial \underline{\underline{A}}}{\partial k_j}\underline{\Phi} - \frac{\partial \underline{f}}{\partial k_j}\right)$$

2.1.3 The merger

Taking the derivative of both sides of the linearized minipermeameter equation (1.5) with respect to the jth element conductivity, and combining with (2.6) yields the expression for the jth weighting function (2.15), which is then subject to the condition that the weighting functions must sum to one (2.3b).

$$(2.15) \qquad \overline{\beta}_j = \frac{dk_{eff}}{dk_j} = \frac{1}{aG_o(b_d)[\Phi_i - \Phi_o]} \frac{d\dot{m}}{dk_j}$$

Since the fraction on the far right hand side of (2.15) is a constant, the weighting functions are readily determined by simply normalizing the sensitivity coefficients to sum to one without multiplying by the constant.

From examination of (2.2), in the limit as the element volumes approach zero, the spatial weighting functions are approximated by (2.16) where element j has centroid located at (r_j, z_j). In order to accurately approximate the point location values of the spatial weighting function, an extremely fine level of element discretization is desired.

$$(2.16) \qquad \text{as} \lim_{V_j \to 0} \quad \beta(r_j, z_j) \approx \frac{\overline{\beta}_j}{V_j}$$

where element j has centroid located at (r_j, z_j)

2.2 Methods

Both the state and adjoint problems were solved by the finite element method. For this minipermeameter problem, that of a semi-infinite domain with the predominance of flow concentrated beneath the tipseal, an important advantage of the chosen method is the ease with which finite elements accommodate non-uniform grid spacing. The equations were derived using the Galerkin formulation of the method of weighted residuals for triangular elements and linear basis functions (Celia and Gray, 1992; Huebner and Thornton, 1982; Wang and Anderson, 1982), as outlined in section 1.2. Since the conductivity matrix, $\underline{\underline{A}}$, is symmetric, only a few additions are needed to extend the program to determine sensitivity coefficients using (2.13) and (2.14). An overview of the extensions are given in the next section, followed by a discussion of numerical considerations.

After the sensitivity coefficients, $\dfrac{d\dot{m}}{dk_j}$, are determined, the condition (2.3b) is applied to determine the weighting functions. Note that since the values are normalized to one, it is not necessary to multiply the derivatives by the constant value proceeding the derivative in (2.15).

2.2.1 Modifications for sensitivity coefficients

For linear problems, it is relatively simple to extend a typical finite element code to handle the adjoint problem and subsequent determination of sensitivity coefficients. Since $\underline{\underline{A}}$ is a symmetric matrix and already available from the state problem, only the

adjoint load vector, $\dfrac{\partial \dot{m}}{\partial \underline{\Phi}}$, needs to be assembled before the additional solution of the

adjoint problem (2.13). Also, the boundary conditions are not a function of the

permeability, so $\dfrac{\partial \underline{f}}{\partial k_j}$ in (2.14) is zero for every element. After the pseudo-potentials

and adjoint states are determined, the only additional work required is assembling the

direct contributions, $\dfrac{\partial \dot{m}}{\partial k_j}$, in (2.14) and using the terms of the matrix of partial

derivatives of the conductivity matrix (each $\dfrac{\partial \underline{\underline{A}}}{\partial k_j}$) and linear algebra operations to

attain the indirect contributions in (2.14).

In the following sub-sections, the schemes for determining the adjoint load vector,

direct contributions, and indirect contributions are outlined. To illustrate the ideas, a

simple example is utilized where the surface beneath the tipseal that receives inflow is

discretized such that flow enters through only four nodes, say nodes 1, 10, 11, and 14.

In this case, the mass flow in, $\dot{m}$, is the sum of the inflow through each of these nodes

(2.17). The equations for the node fluxes (2.18) can be quickly determined from back-

substitution and rearrangement of the state matrix equation (1.16). ,

$$(2.17) \qquad \dot{m} = \dot{m}_1 + \dot{m}_{10} + \dot{m}_{11} + \dot{m}_{14}$$

$$(2.18) \qquad \underline{\dot{m}} = \underline{\underline{A}}\underline{\Phi} - \underline{f}$$

2.2.1.1 Direct Contribution

The direct contributions will be non-zero for only those elements which directly impact the flow through the upper constant head surface inside the tipseal - the elements which share the constant potential nodes along the inflow surface. Using the previous example, the direct contribution for the eth element, is then:

$$(2.19) \qquad \frac{\partial \dot{m}}{\partial k_e} = \frac{\partial \dot{m}_1}{\partial k_e} + \frac{\partial \dot{m}_{10}}{\partial k_e} + \frac{\partial \dot{m}_{11}}{\partial k_e} + \frac{\partial \dot{m}_{14}}{\partial k_e}$$

For triangular elements, a maximum of two nodes from a single element may be located on the inflow surface, so a maximum of two contributions on the right hand side of (2.19) will be non-zero. Employing (2.18), a vector of the partial derivatives of all nodal fluxes with respect to the eth element permeability can be written as (2.20), where we are only interested in the entries that apply to the inflow surface. For the example problem, these entries correspond to the right hand side of (2.19).

$$(2.20) \qquad \frac{\partial \dot{m}}{\partial k_e} = \frac{\partial \mathbf{A}}{\partial k_e} \Phi - \frac{\partial \mathbf{f}}{\partial k_e}$$

Two important facts simplify finding the terms in (2.20). The first observation is that the load vector, which consists of entries for constant flux (equal to zero) nodes, is independent of the element permeability and therefor $\frac{\partial \mathbf{f}}{\partial k_e}$ is always zero. The second observation involves recalling that the conductivity matrix was assembled on an element by element basis (1.20), and only the eth element contributions to the

conductivity matrix are dependant on the eth element permeability. Applying these rules, the fastest way to determine the direct contribution for all elements is to iterate through the nodes on the inflow surface. For each element, e, containing a surface node, i, the ith nodes portion of the eth element's direct contribution is then:

$$(2.21) \qquad \frac{\partial \dot{m}_i}{\partial k_e} = \frac{\partial \mathbf{A}^e_{i,i}}{\partial k_e} \Phi_i + \frac{\partial \mathbf{A}^e_{i,j}}{\partial k_e} \Phi_j + \frac{\partial \mathbf{A}^e_{i,m}}{\partial k_e} \Phi_m$$

where the element values, $\mathbf{A}^e_{i,L}$ for $L = i, j, m$, can be found by simple differentiation of (1.20).

2.2.1.2 Adjoint Load Vector

The adjoint load vector is the partial derivative of the mass influx with respect to the change in potential ($\frac{\partial \dot{m}}{\partial \underline{\Phi}}$). Since the total flow may be examined as the inflow through each of the nodes beneath the tipseal chamber, we may determine our contributions to the load vector by taking the derivative of the total flow with respect to each pseudo-potential value. Applied to our example, the jth entry in the load vector is given by:

$$(2.22) \qquad \frac{\partial \dot{m}}{\partial \Phi_j} = \frac{\partial \dot{m}_1}{\partial \Phi_j} + \frac{\partial \dot{m}_{10}}{\partial \Phi_j} + \frac{\partial \dot{m}_{11}}{\partial \Phi_j} + \frac{\partial \dot{m}_{14}}{\partial \Phi_j}$$

For our problem, this is further simplified by recognizing that 1) the adjoint state load vector entries are non-zero only for nodes comprising and directly connected to the upper surface, and 2) the flow equation load vector has no dependence on the pseudo-potentials so $\dfrac{\partial r_j}{\partial \Phi_j}$ is zero for all nodes, and 3) the back substitution associated with the coefficient matrix is linearly multiplied by the pseudo-potentials. This results in a rapid assembling of the adjoint state load vector by looping through the nodes located on the inflow surface and simply adding the appropriate coefficient matrix entries. For our example, the jth entry is:

$$(2.23) \qquad \frac{\partial \dot{m}}{\partial \Phi_j} = A_{1,j} + A_{10,j} + A_{11,j} + A_{14,j}$$

where $A_{i,j}$ is the entry in the ith row and jth column of the coefficient matrix $\underline{\underline{A}}$.

2.2.1.3 Assembling Indirect Contribution

After the adjoint load vector is assembled, and the adjoint state vector ($\underline{\psi}^{*}$) determined, the indirect contribution for each element needs to be determined. For the eth element, this scalar is derived from solving $\underline{\psi}^{*T} \dfrac{\partial \underline{\underline{A}}}{\partial k_j} \underline{\Phi}$. As discussed for the direct contributions, the partial of the conductivity matrix with respect to the eth element is only non-zero for the portion of the entries derived from element e. By iterating through each of the elements, the indirect contribution for element e, comprised of

nodes i, j, and m, is then quickly assembled from (2.24), where the element values,

$\dfrac{\partial A^e_{i,L}}{\partial k_e}$ for $L = i, j, m$, can be found by simple differentiation of (1.20).

$$\underline{\psi}^T \frac{\partial A}{\partial k_e} \underline{\Phi} = \left(\frac{\partial A^e_{i,i}}{\partial k_e} \Phi_i + \frac{\partial A^e_{i,j}}{\partial k_e} \Phi_j + \frac{\partial A^e_{i,m}}{\partial k_e} \Phi_m \right) \psi_i^*$$

$$(2.24) \qquad + \left(\frac{\partial A^e_{j,i}}{\partial k_e} \Phi_i + \frac{\partial A^e_{j,j}}{\partial k_e} \Phi_j + \frac{\partial A^e_{j,m}}{\partial k_e} \Phi_m \right) \psi_j^*$$

$$+ \left(\frac{\partial A^e_{m,i}}{\partial k_e} \Phi_i + \frac{\partial A^e_{m,j}}{\partial k_e} \Phi_j + \frac{\partial A^e_{m,m}}{\partial k_e} \Phi_m \right) \psi_m^*$$

2.3 Results

A tipseal with ratio $b_d = \dfrac{a}{b} = 2$, inner tipseal radius $a = 1$, applied potential $\Phi_i = 1$,

and ambient potential $\Phi_o = 0$ was simulated. A homogeneous, isotropic permeability

of 1 ($k_r = k_z = 1$) was also used. For the homogenous case, the weighting functions

are independent of the magnitude of the permeability. To insure that truncation error

and boundary conditions did not effect the weighting functions, multiple simulations

were performed for various domain sizes and discretization levels. Since flow is

concentrated near the tipseal boundary, it is necessary to finely discretize this area to

the level that a more fine discretization does not significantly increase the inflow rate.

Although our finite element simulation estimated the Goggin factor accurately at

rougher discretization levels, in the end an extremely fine discretization was employed

for reasons relating to the smoothness of the sensitivity coefficient field (discussed later). The grid utilized in the simulations had dimensionless radius (R_D,) of 10.7, and dimensionless thickness (Z_D) of 14.3, with discretization in the near tipseal region as fine as 0.00036 dimensionless units. As a result, no greater than 2.8 % of mass flux entered through any node, and the resulting Goggin factors were nearly exact at 5.099 ± 0.005 (compared to the unpublished analytical solution of Kerr and Wilson (personal communication, 1998)) with a mass balance error less than 0.0022 %. To further insure the semi-infinite geometry is represented, the weighting functions calculated for different sets of "infinite" boundary conditions were compared and showed essentially no difference in the near field region.

A contour of the pseudo-potentials appears in Figure 2.1a. The spacing of pseudo-potential lines increases with distance from the tipseal, and does not extend nearly as far in the radial direction as along the z-axis. For the simulation contoured in Figure 2.1, the far boundary conditions were constant pseudo-potentials. Use of no-flow boundary conditions resulted in pseudo-potential contour lines that differed only slightly in the far field portion of the figure.
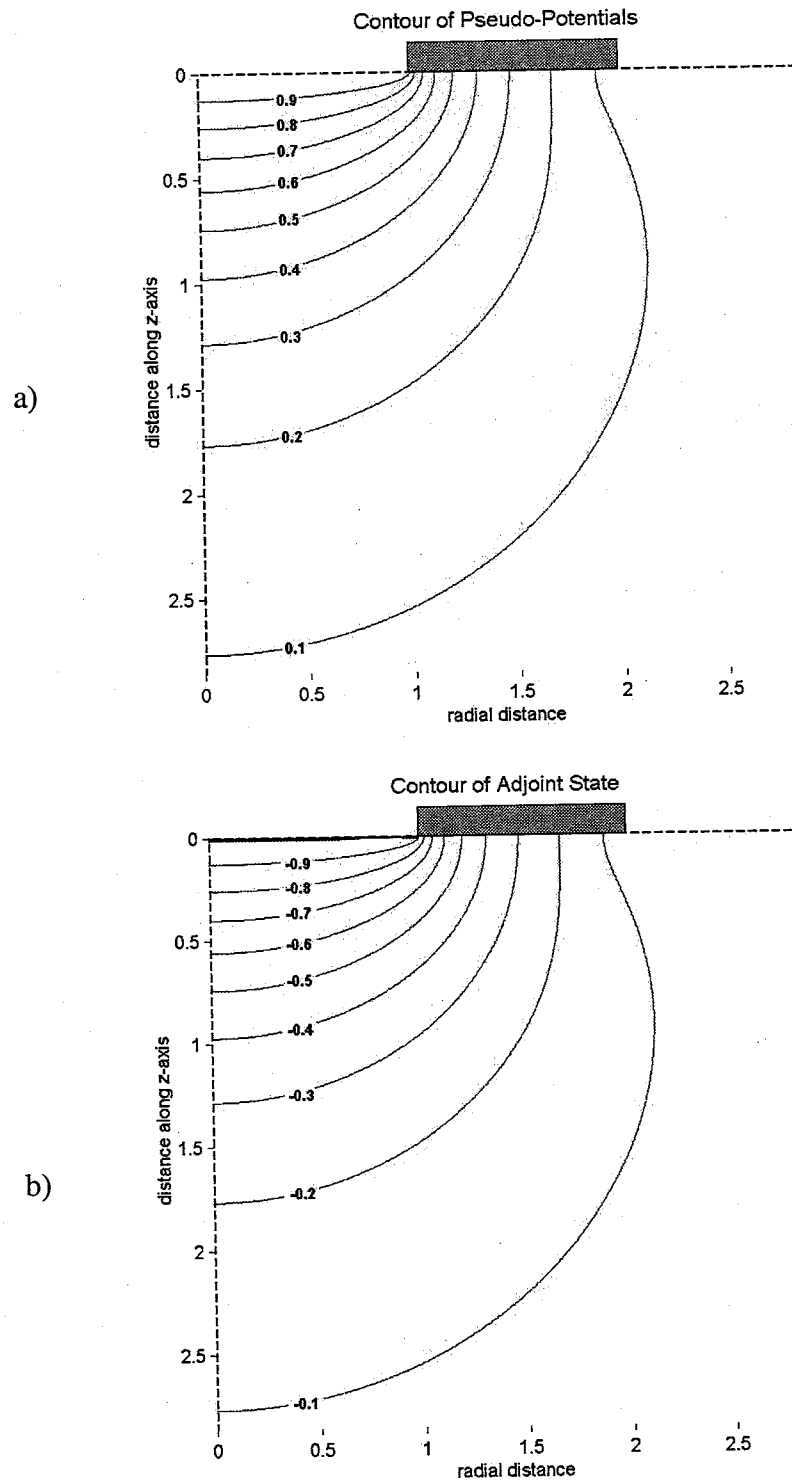
Figure 2.1 - Contours of the (a) pseudo-potential and (b) adjoint state fields. The no-flow region of the tipseal is represented by the shaded rectangle.

Due to the unit values used in the simulations, the adjoint state field (Figure 2.1b)

looks identical to the pseudo-potential field, except in the very near field. If the

applied pseudo-potential beneath the tipseal doubled, the contour labels in Figure 2.1a

a would double, but the adjoint state result would remain the same. This is consistent

with the definition of adjoint state, since we would expect the total inflow to change

the same (although percentage wise have a different impact) due to a unit injection.

Note the solid dark area directly beneath the tipseal chamber in Figure 2.1b. The

adjoint state boundary condition along this length is a constant adjoint state of zero.

Since flow is induced across the constant head boundary, a unit injection of air at this

boundary would have no effect on the nodal flow values.

2.3.1 Weighting functions

Since each permeability is associated with an element, applying adjoint state analysis

results in a volumetric weighting function which is related to the size of the element.

Results are presented here in terms of both the volumetric weighting functions $\overline{\beta_j}$ and

the point value spatial weighting functions estimated at the element centroid

$\beta\,(r,z,\theta)$. The volumetric weighting functions lend themselves to a discussion of the

volume of rock interrogated by the minipermeameter, while the spatial weighting

function relates to the importance of small heterogeneities within the flow field.

For both weighting functions, the locations directly beneath the inside and outside

edges of the tipseal are of greatest importance, with the largest values beneath the

inner edge (Figures 2.2 and 2.5). This follows intuitively since directly beneath the conformable tipseal represents the shortest flow lengths. A change in conductivity here has the significant effect on either driving flow deeper or shortening of the flow field. At larger distances, the nature of the field becomes increasingly hemispherical. Representing the shortest flow path, we would expect that the bulk of the mass flow would be in this near tipseal region, which is confirmed by the stream potentials (Figure 2.3).

2.3.2 Volumetric Weighting Functions, $\overline{\beta_j}$

Since each of the elements in the axisymmetric simulation represent a volume of rock with a uniform permeability, k_j, the resulting weighting function for each element, $\overline{\beta_j}$, includes the effect of the different rock volumes. In fact, due to the linear basis functions, the volume of the element ($2\pi \overline{R} A^e$) appears explicitly within both the direct and indirect contributions to the sensitivity coefficients. Including the volumetric effect, Figure 2.2 is a grayscale plot illustrating the cumulative contribution of different regions to the effective permeability measurement. To account for the variation in element areas (not volumes), the volumetric values ($\overline{\beta_j}$) were cumulatively summed in order of their area normalized value ($\dfrac{\overline{\beta_j}}{A^e}$). This accounts for the influence of the different element areas (introduced by irregular discretization). Added in this manner,
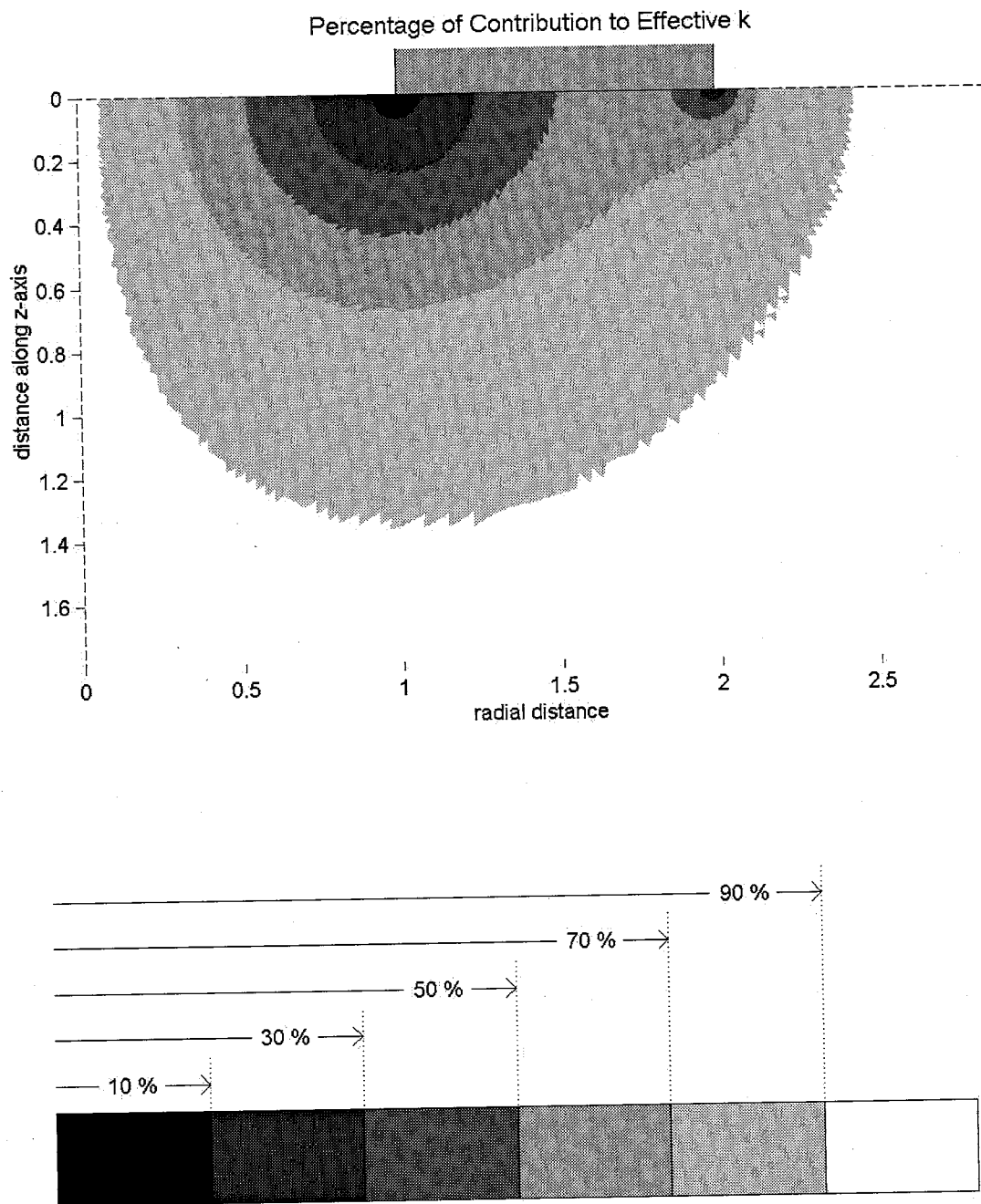
Figure 2.2 - Greyscale showing the cumulative contribution of the volumetric weighting functions (added by element), $\overline{\beta_j}$, to the effective permeability.

the smallest volume for a particular percent of the weighting function is determined. For example, 10% of the total contribution to the effective permeability is contained in the tiny regions directly beneath the inner and outer edges of the tipseal. Figure 2.2 also shows that the volumes along the z-axis appear as offering a relatively negligible contribution to the effective permeability.

Figure 2.3 is a contour of the stream potentials, where the area between consecutive contours contains 10% of the total inflow. As can be seen, a large percentage of the flow is contained in the relatively small volume directly beneath the tipseal. For comparison with the results of other investigations, Figure 2.4 shows the percentage of the weighting functions contained within different sample volumes. We used a right cylinder centered around the origin and described by a single dimensionless length $\left(R_D = L_D \right)$, and a hemisphere beneath the tipseal centered at $\left(R_D = 0, L_D = 0 \right)$. Since the largest weights are located along the surface near the tipseal, a similar pattern is observed as the dimensionless confining coordinate increases. 95% and 99% of the weighting function are contained within a cylinder with $R_D = L_D = 2.3$ and 3.71, respectively, or a hemisphere with dimensionless radius (equal to $(R_D^2 + L_D^2)^{1/2}$) of 2.5 or 4.16, respectively.
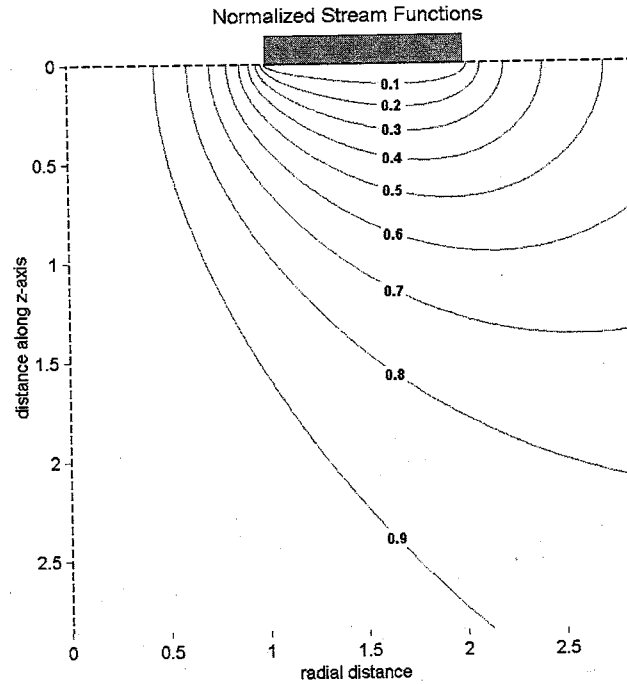
Figure 2.3 - Normalized stream functions. The volume between consecutive contours contains 10 % of the inflow from the minipermeameter, and the contour labels indicate the cumulative inflow beginning from the tipseal no-flow boundary (shaded rectangle).
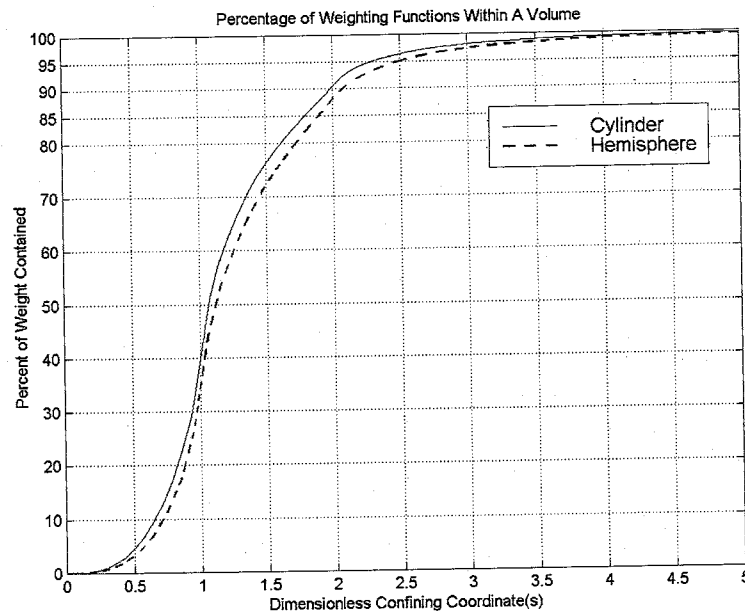
Figure 2.4 - Percentage of weighting function contained in right cylinder or hemisphere by dimensionless confining coordinate. The confining coordinate is $R_D = Z_D$ and $\left(R_D^2 + Z_D^2\right)^{1/2}$, for the cylinder and hemisphere, respectively.

2.3.3 Spatial Weighting Functions

As the volumes of the elements become sufficiently small such that the spatial weighting function, $\beta(r,z,\theta)$, is essentially constant throughout the volume, the spatial weighting function may be estimated from the volumetric weighting function (2.16). Therefor, as the discretization becomes finer, the surface becomes increasingly smooth. Figure 2.5 shows a contour of these planar weighting functions expressed as log base 10 values, using a constant contour interval of 0.25. Prior to the log transformation, integration of the plane of spatial weighting functions (over the entire simulated domain) about the axis of symmetry equals one. The effect of the larger elements with distance from the tipseal appear as wavy contours. The locations directly under the tipseal edges represent the most important locations to the effective permeability measurement, and the contours of the spatial weighting function become increasingly hemispherical with distance from the origin.

Since the fine discretization leads to a good approximation of spatial weighting function point values, correlation with the results of the state solution were attempted. Treating the numerical solution in dimensionless form (1.10-1.13), dimensionless spatial weighting functions $\beta_d(x_d, r_d, \theta)$ are derived after dividing through by the dimensionless volume (analogous to (2.16)). Figure 2.6 is a graph of point values of the dimensionless spatial weighting function estimated at the centroid of each element versus the resulting correlation equation (2.25).

2-D Plane of Spatial Weighting Function, $\log_{10} \beta (r,z)$

distance along z-axis

-1
-1.5
-2
-2.5
-3
-3.5
-4

radial distance
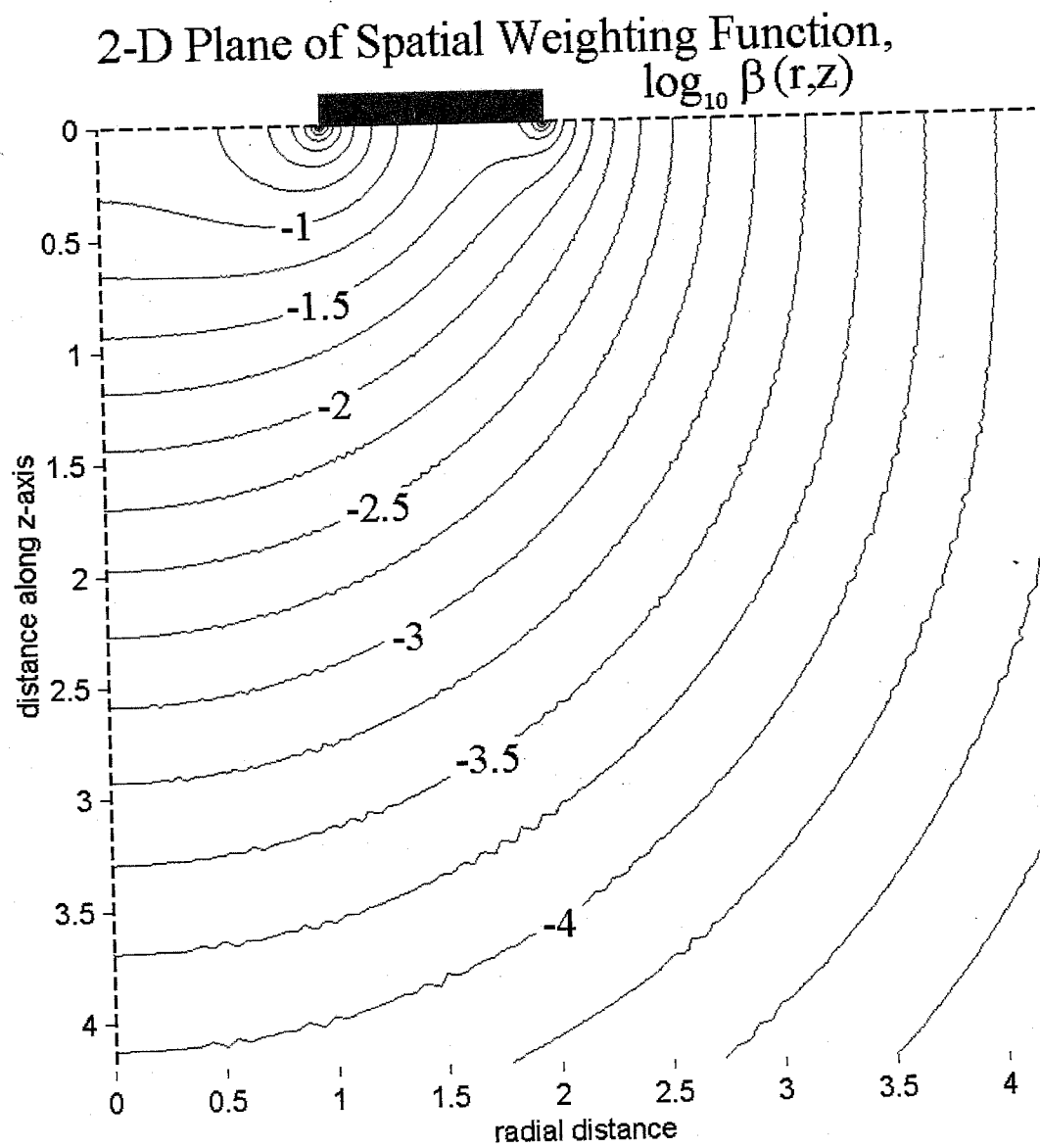
Figure 2.5 - Two dimensional (r-z) plane of spatial weighting functions, $\beta(r,z,\theta)$, created by contouring the point values estimated at the element centroids. The values are displayed as $\log_{10} \beta(r,z,\theta)$, with a constant contour interval of 0.25.

$$(2.25) \qquad \beta_d(x_d, r_d, \theta) \approx \frac{1}{G_o} \left| \nabla \Phi_d \right|^2$$

$$\text{where:} \quad \nabla \Phi_d = \frac{\partial \Phi_d}{\partial r_d} \hat{r}_d + \frac{\partial \Phi_d}{\partial z_d} \hat{z}_d$$

A near perfect correlation is attained, with a standard deviation from the 1:1

relationship of 0.00084. Additionally, the proposed correlation equation is also

dimensionless. Transforming into dimensional terms, the correlation equation

becomes:

$$(2.26) \qquad \beta(x, r, \theta) \approx \frac{1}{aG_o} \left| \frac{\nabla \Phi_d}{\Phi_i - \Phi_o} \right|^2$$

$$\text{where:} \quad \nabla \Phi = \frac{\partial \Phi}{\partial r} \hat{r} + \frac{\partial \Phi}{\partial z} \hat{z}$$

Both sides of (2.26) have the familiar $[L^{-3}]$ of the spatial weighting function. Since

unit values were used, some additional simulations with different geometry (but $b_d=2$)

and pressure values were used to confirm the correlation equation. The equation

strongly suggests that the square of the potential gradient is equal to the spatial

weighting function. A very interesting aspect of this correlation is the appearance of

the Goggin factor (G_o), which never explicitly enters the calculations to determine the

spatial weighting functions.

Weighting Function Correlation
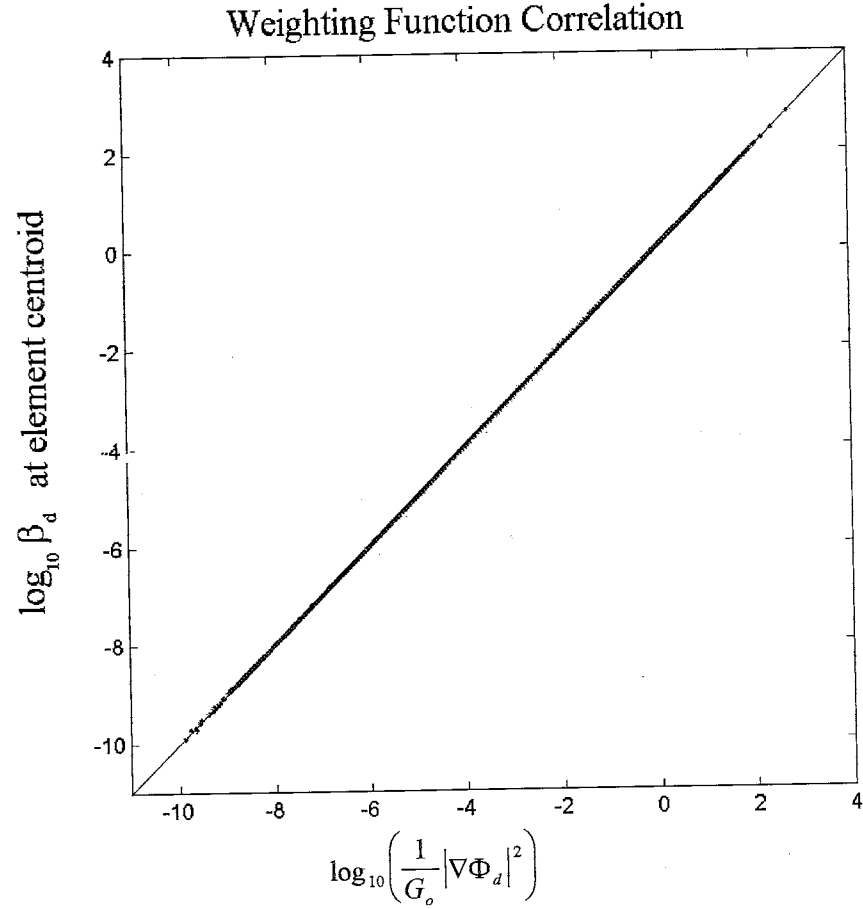
Figure 2.6 - Spatial weighting functions versus the correlation equation. The 39,150 data points appear as dots along the 1:1 solid line.

2.4 Conclusions

In this investigation, the methodology for utilizing adjoint state sensitivity analysis to determine linear weighting functions is developed, and implemented for the minipermeameter. It was shown that extension of a flow code to handle the adjoint state problem is relatively straightforward, and the finite element equations can be readily manipulated for determination of the sensitivity coefficients. This procedure

offers a straightforward way to assess the relative importance of regions which contribute to the effective property that an instrument yields.

For a homogeneous field, these spatial weighting function values (obtained at element centroids) represent the correct weights for any power law averaging process (arithmetic, geometric, harmonic, etc.). As the sample becomes increasingly heterogeneous, the choice of averaging process would then be expected to yield increasingly variant weights. It is important to note that, while this particular investigation does not lend itself to determining the correct averaging procedure for the divergent flow geometry of the air permeameter, it does allow us to determine the relative importance of different regions under the assumptions for which the minipermeameter equation was developed.

For the minipermeameter, both volume averaged and point value weighting functions were determined, and examined to give insight into the extent and relative importance of the regions sampled by the minipermeameter. Both types of weighting functions show that the region beneath the no-flow boundary of the tipseal has the largest influence on the effective permeability yielded by the instrument. In particular, the inner and outer edges of the region have the greatest impact.

The extent of the region interrogated by the minipermeameter was estimated by summing the volumetric weighting functions as a function of volume. These suggest that 95% of the region contributing to the effective permeability is contained within a

right cylinder characterized by a dimensionless radius and length of 2.3 or a

hemisphere characterized by a dimensionless radius of 2.5. Approximately 99% of the

weighting function is contained in a cylinder with dimensionless lengths 3.71 or a

hemisphere of 4.16. Comparison between the dimensions containing 95 and 99% of

the weighting functions suggests that the effective permeability is already becoming

very insensitive to the region beyond the coordinate bounding the 95% contribution.

With this in mind, the values obtained are in agreement with those obtained by Suboor

and Heller (1995): R_D=2.88 and Z_D=3.50 for a 1% change, and numerical results of

Chen: R_D=4.0 for a 0.8% - 3% change and R_D=Z_D=2.5 for a 5.8-17.8 % change.

Additionally, the point value weighting functions were accurately estimated to give

insight into the importance of local heterogeneities throughout the flow field. A very

interesting correlation relating the spatial weighting functions and mass flux

relationships is observed. Confidence in the proposed equations is strengthened by the

agreement of the units with that of the spatial weighting functions. Also interesting to

note is the appearance of the geometric factor, despite the fact it never enters explicitly

into the calculations that lead to the weighting functions. Since the adjoint state must

be calculated by solving a large system of equations, it is not possible to determine if

the correlation equation arises directly from the finite element equations. In fact,

inspection of the balance of the manipulated finite element equations (other than the

adjoint term), and the fact that the geometric factor and inner radius appear in the

correlation equation, suggest that it will not.

Further work needs to be done to establish whether the derived correlation holds up for other tipseal ratios, and whether the geometric factor for these ratios explicitly appears. Additionally, applying this technique to the problem of saturated flow to a well would offer a chance for further insight and the opportunity to contrast the obtained weighting functions with the numerical studies of other investigators.

3. Determination of Geometric Factors for a Layered Permeability System

Currently, minipermeameters are utilized to determine the sample permeability under the classical assumptions for a single homogenous material, or when the near field is felt to approximate these conditions. In this chapter, new geometric factors are presented for the two layer permeability system. Utilized in the standard permeameter equation (1.9), these new geometric factors (G_D) can be used to determine the permeability of one layer when independent measurements of the upper layer thickness (d) and permeability of second layer are available. This both expands the possible range of minipermeameter applications, and yields further insight into the appropriate application of the minipermeameter under classical assumptions. In particular, the geometric factors derived in this investigation should prove useful for investigating the permeability across narrow faults (Sigda et al., 1999).

The layered permeability system is shown schematically in Figure 3.1. This system has two parallel layers, which have (or appear to have) different permeability values. The upper layer is characterized by a thickness, d, and permeability k_T, and the lower layer has permeability k_B. This geometry has been encountered in both field and laboratory investigations of permeability alterations due to faulting. To use the new geometric factor, the upper layer thickness and an independent measurement of the permeability of one of the two layers is needed. For determining the permeability of a narrow fault

deformation band (k_T), this is accomplished by 1) measuring the deformation band

thickness, and 2) obtaining a minipermeameter measurement on the host rock by either

removing the upper layer to give surface exposure or by making a measurement on the

adjacent host rock. Other scenarios for the layer system also exist, such as

investigating the permeability alterations associated with surface weathering or sample

preparation, that could be crudely modeled assuming the layered geometry.
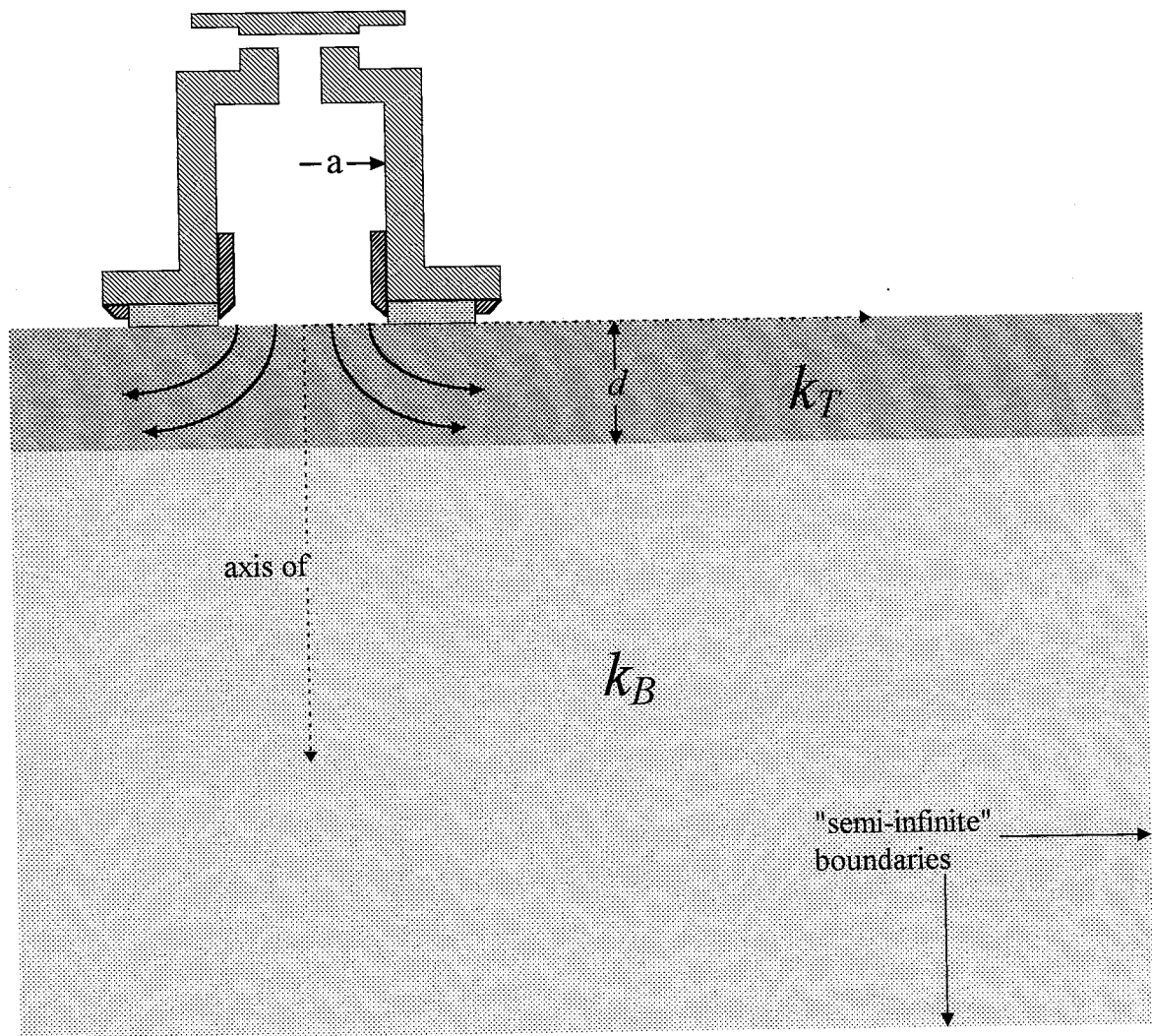
Figure 3.1 - Two-layer permeability system. The upper layer has thickness, d, and permeability k_T. The lower layer has "infinite" thickness and permeability k_B.

In addition to the new geometry, this study yields insight into the appropriate use of the minipermeater for field situations. An important consideration in performing field measurements is that boundary conditions or physical anomalies (such as root tubules) do not significantly effect the flow regime. Even in the absence of a known permeability value for the deeper "layer", the curves generated by this study can be used to quantify appropriate distances at which the impact of a second layer do not substantially violate the assumption of a single homogenous layer. An example of this is the presence of a drying front (representing the beginning of a second permeability layer) introduced when an "outcrop" face is opened by excavation. In this case, the face is typically allowed to dry for an extended period before permeametry begins. Assuming that the drying front is self-stabilizing (implying a fairly abrupt transition between moisture contents), then an appropriate distance for the front to recede from the open face may be estimated based on the tipseal radius and required accuracy.

The primary motivation for this work - the use of the minipermeameters in investigations of fault zone permeability, is discussed in the next section. This is followed by sections discussing the methodology utilized, results and discussion, and conclusions. In the discussion section, two methods are proposed that provide for easy inversion of the raw data.

3.1 Investigating fault permeability

An area of developing interest are the hydrologic impacts of faulting in sedimentary rocks. Although major faults that extend into sedimentary rocks are sometimes addressed, the effects of associated deformation bands, are not often recognized. These deformation bands, whose minor displacements probably have only very localized impacts on flow, could significantly alter flow due to reduction in permeability associated with the change in petrophysical properties (Aydin and Antonellini, 1994; Fowles and Burley, 1994; Sigda et. al, 1999).

Fowles and Burley (1994) examined permeability variations associated with cataclastic slip bands (deformation bands) in high porosity, well indurated, sandstones in north-west England and south-west Scotland. Using 75 one inch diameter cores taken both parallel and perpendicular to the bands, they found decreases in permeability up to 4 orders of magnitude. Since the band thickness was smaller than the cores, the resulting permeability values are actually an average of deformation band and host rock permeability.

In attempting to isolate fault permeability, several researchers have utilized minipermeameters in their investigations of faults. Sigda et. al (1999), used a syringe based air minipermeameter to investigate alterations in permeability associated with faulting in poorly consolidated sandstones in central New Mexico. For two faulted areas (one with and one without a clay-rich core), permeability was measured both parallel and normal to the fault structure. They describe permeability decreases in the

deformed material between two and three orders of magnitude, with the larger

decreases for measurements normal to the band of deformation. Their study also

notes that some fault permeability values may be biased high, due to the influence of

the higher permeability host rock within the zone of permeameter investigation.

Aydin and Antonellini (1994) utilized a minipermeameter to investigate fault

permeability in well indurated sandstones in Arches National Park, Utah. Based on

Goggin's geometric factors, they estimated a depth of investigation of 1 cm

(dimensionless depth of 2). For deformation bands thinner than 1 cm, the

measurements were corrected using a harmonic mean average based on approximating

the geometry to be two-dimensional radial flow in a plane parallel to the

minipermeameter axis (see Figure 5c, Antonellini and Aydin, 1994). This geometry

was chosen since it yielded corrected permeability values closest (within a factor of

five) to the permeability values in uncorrected (thicker than 1 cm) samples. They

observed changes in permeability up to 4 orders of magnitude, with an average

decrease in permeability of three orders of magnitude.

Demonstrating the impact of narrow faults on the flow regime, Aydin and Antonellini

(1994) also calculated average permeability values for "grid blocks" of different scales

by considering the number, distribution, and thickness of deformation bands (which

they define as 0.5-2 mm thick) across the Moab sandstone. The resulting average

permeability values decreased (relative to the host rock) 1 to 2 orders of magnitude for

1 m grid blocks, and about an order magnitude for grid blocks of scale 20 m.

These investigations demonstrate that decreases in permeability associated with narrow faults may have significant controls on hydrologic processes. They also illustrate the difficulty in obtaining accurate permeability measurements of narrow deformation bands. Since the scale of characterization is much smaller, and the controls on hydrologic impact such as the areal density, geometry, and permeability are not well understood (Sigda et al., 1999), further study is needed to assess these hydrologic impacts.

In other studies regarding the spatial variation of permeability, the portable minipermeameter has proven to be an ideal instrument for quickly obtaining a large number of accurate measurements. Using the newly determined geometric factors will now provide for the quick, accurate determination of deformation band permeability for both field and laboratory studies.

3.2 Methods

The transformed governing equation (1.5) which describes ideal-gas flow was solved numerically using the previously described finite element code. For simplicity, the number of variables effecting the geometric factor were reduced, and then relationships between the remaining variables and the geometric factor were determined. To insure accurate solution, several modeling issues concerning mesh discretization and domain size were addressed. The resulting relationships were then

explored, and methods for practical application of the two layer geometric factor were determined.

3.2.1 Approach

The general form of the standard permeameter equation (1.1) was assumed to be appropriate (and checked) for the two-layered system, where G_D is the new geometric factor for the two layered permeability system (3.1). Goggin et al. (1988) found the single layer geometric factor to be dependant on the dimensionless sample size and the tipseal radius ratio. For this investigation, the focus was establishing the relationships effecting the geometric factor, and determine whether or not a simple method of inverting permeameter data for the layered system was possible. Therefore, for simplicity, the dependence on the sample size was eliminated by assuming that all flow was into a semi-infinite halfspace. This assumption should not effect practical minipermeameter use, as long as tipseal or sample size are chosen appropriately. Additionally, a single tipseal ratio, $b_d = 2$, was utilized in all simulations. In the future, this approach will be applied to determine the geometric factors for other tipseal ratios, as well as investigating relationships between different tipseal values.

$$(3.1) \qquad k_{eff} = \frac{\dot{m}}{a G_D (b_d, D, K_R)[\Phi_i - \Phi_o]}$$

where $\dot{m}$ = mass flow rate into the sample [M t^{-1}]

Φ_i $\equiv$ applied pseudo-potential beneath

the tipseal $[M\,t^{-1}L^{-3}]$

Φ_o $\equiv$ "ambient" pseudo-potential $[M\,t^{-1}L^{-3}]$

$G_D(b_d, D, K_R)$ $\equiv$ two layer geometric factor

D $\equiv$ dimensionless depth to top of lower

permeability layer, $= \dfrac{d}{a}$

K_R $\equiv$ ratio of upper layer permeability to

lower layer permeability, $= \dfrac{k_T}{k_B}$

The two-layer geometric factor is also a function of the two dimensionless ratios:

upper layer thickness to the inner tipseal radius (D), and upper material permeability to

lower layer permeability (K_R). After validating the accuracy of the numerical solution

(discussed in the following section) for each mesh, the relationships were determined.

A method was then developed so that permeability values for layered systems can be

quickly inverted.

3.2.2 Numerical Issues

All geometric factors presented here were determined for the case of flow into a semi-

infinite half-space. To achieve this numerically, it is necessary to use a domain in

which these "infinite boundaries" are located at distances such that simulation results

are not significantly impacted. To determine acceptable locations, simulations were

performed where both distant boundaries had constant potential conditions or both

had no-flow conditions. Like Chen (1992), it was assumed that the true semi-infinite geometric function would lie between the geometric functions produced by these end-case simulations.

A second important consideration was the element discretization level required to minimize errors in the geometric factor. To minimize truncation error, small elements were necessary near the tipseal edges where inflow and outflow are concentrated, and along the interface between the distinct permeability layers. These discretization levels were determined by solving the classical one permeability minipermeameter problem. By using increasingly finer discretizations, an acceptable discretization level was determined when the geometric factor yielded by the simulation was within roundoff error of the analytical solution, $G_o = 5.10$ (Kerr and Wilson, pers. com., 1998). This discretization served as an upper bound, and the meshes that were ultimately utilized had discretization levels at least an order of magnitude more detailed in regions near the tipseal. It was assumed that the ultra-fine discretization levels ultimately used near the tipseal was also acceptable for the material interface.

It is also important to note that the above issues - boundary locations and mesh discretization, should not be addressed independent of each other. If the mesh discretization is examined while the "infinite" boundary conditions are effecting flow, the resulting geometric functions will converge to a value other than the true geometric factor. Alternatively, if a particular discretization level is acceptable, and then boundary locations are determined, the simulation converges to a different

geometric function. For most investigations, the differences in these values is not important. Since we are attempting to identify and characterize relationships for the two layer geometric factor, mesh calibration to a unique value was important. Evidence that the most accurate geometric factor for b_d=2.0 reported is, in fact, 5.10 (the proposed analytical solution), was found in the fact that as meshes became larger and more finely discretized, the values converged and settled on that value.

3.3 Results & Discussion

Assuming the same form of the traditional permeameter equation (3.1), the dual layer geometric factor (G_D) was found to be independent of the applied potentials and mass inflow values. For our restricted geometry (semi-infinite sample and tipseal ratio, b_d, of 2), it was observed to be dependant on only two dimensionless values: the ratio of depth to the inner tipseal radius (D), and the ratio of the two permeability values (K_R). Ultimately G_D was determined for 133 different combinations of K_R and D. Table 3.1 shows these values, and a detailed listing of all simulations is given in Appendix A. For all simulations, the mass balance error was less than 0.015 %.

		0.1250	0.2143	0.3571	0.4286	0.5000	1.0000	1.4286	2.0000
	0.0001	27.872	17.466	11.701	10.277	9.271	6.454	5.754	5.401
	0.00075		17.423	11.684					
	0.001	27.710				9.258	6.450		
	0.002	27.533	17.342	11.652	10.242	9.244	6.446	5.751	5.400
LOWER	0.01	26.224	16.849	11.453	10.098	9.135	6.416	5.737	
layer	0.02	24.800	16.285	11.219	9.928	9.006	6.379	5.720	
more	0.05	21.455	14.857	10.600	9.471	8.654	6.278	5.678	
permeable R	0.1	17.703	13.086	9.788	8.869	8.191	6.137	5.609	5.335
	0.167	14.475	11.361	8.917		7.661	5.997	5.532	
	0.25	11.894	9.843	8.094	7.556	7.143	5.813	5.454	5.265
	0.5	7.978	7.258	6.550	6.312	6.123	5.473	5.287	
	1	5.099	5.099	5.099	5.098	5.098	5.102	5.102	5.103
	2	3.270	3.602	3.995	4.146	4.275	4.775	4.936	
	4	2.209	2.683	3.273	3.509	3.712	4.537	4.813	4.967
UPPER	6	1.828	2.344	2.998	3.263	3.493	4.440	4.763	
layer	10	1.510	2.059	2.764	3.052	3.303	4.355	4.718	4.922
more K_R	50	1.113	1.699	2.464	2.780	3.058	4.242	4.659	4.893
permeable	100	1.062		2.424					4.890
	500		1.615	2.393	2.715	2.999	4.215		
	1000							4.643	
	10000	1.012	1.607	2.385	2.708	2.993	4.212		4.886

Table 3.1 - Two layer geometric factors, G_D, for "semi-infinite" sample and tipseal ratio (b_d) of 2.0. G_D is a function of the dimensionless thickness of the upper layer, D, and the ratio of the upper layer permeability to the lower layer permeability, K_R.

Ultimately nine production meshes were required to identify relationships and give adequate coverage of the range of expected two layer geometries. A description of these meshes is given in Table 3.2. Values for the geometric factor for $D > 2.0$ were not investigated since there is little deviation (less than 6%) from the single layer geometric factor, G_o, regardless of the permeability ratio. Values for geometric factors for $D < 0.125$ were also not determined, since the geometric factor is becoming very sensitive to the permeability ratio. For this case, it is recommended that a smaller tipseal be utilized. Also note that the upper layer in meshes CCdual and FFdual have the same dimensionless thickness (D).

mesh	dimensionless				number of	
	D	R_D	Z_D	del r_D	Nodes	Elements
JJdual	0.125	12.50	16.67	4.17E-04	29202	57381
EEdual	0.214	10.71	14.29	3.57E-04	15496	30190
CCdual	0.357	10.71	14.29	3.57E-04	19969	39150
FFdual	0.357	21.43	28.57	7.14E-04	20741	40739
GGdual	0.429	10.71	14.29	3.57E-04	21263	41735
DDdual	0.500	10.71	14.29	3.57E-04	22418	44043
IIdual	1.000	21.43	28.57	7.14E-04	27788	54820
MMdual	1.429	21.43	28.57	7.14E-04	25984	51214
NNdual	2.000	28.57	34.29	7.14E-04	21116	41479

Table 3.2 - Description of production meshes. D represents the dimensionless thickness of the upper layer, del r_d indicates the nodal spacing at the edges of the tipseal, and R_D and Z_D describe the (dimensionless) radius and thickness, respectively, of the domain.

For all production simulations, the "infinite" boundary conditions had very little effect on the geometric factors. For the case when the upper material is more permeable than the lower material ($K_R > 1$), flow is focused in the upper layer. In this case, the boundary conditions cause little variation in the flow field and the geometric factor was not effected. Figure 3.2 presents the pseudo-potential and streamlines for $K_R = 50$ and $D = 0.357$, for constant potential (Figure 3.2a) and zero flux (Figure 3.2b) boundary conditions. Essentially no difference is observed in the distribution of pseudo-potentials (dashed lines) or streamlines (solid lines).
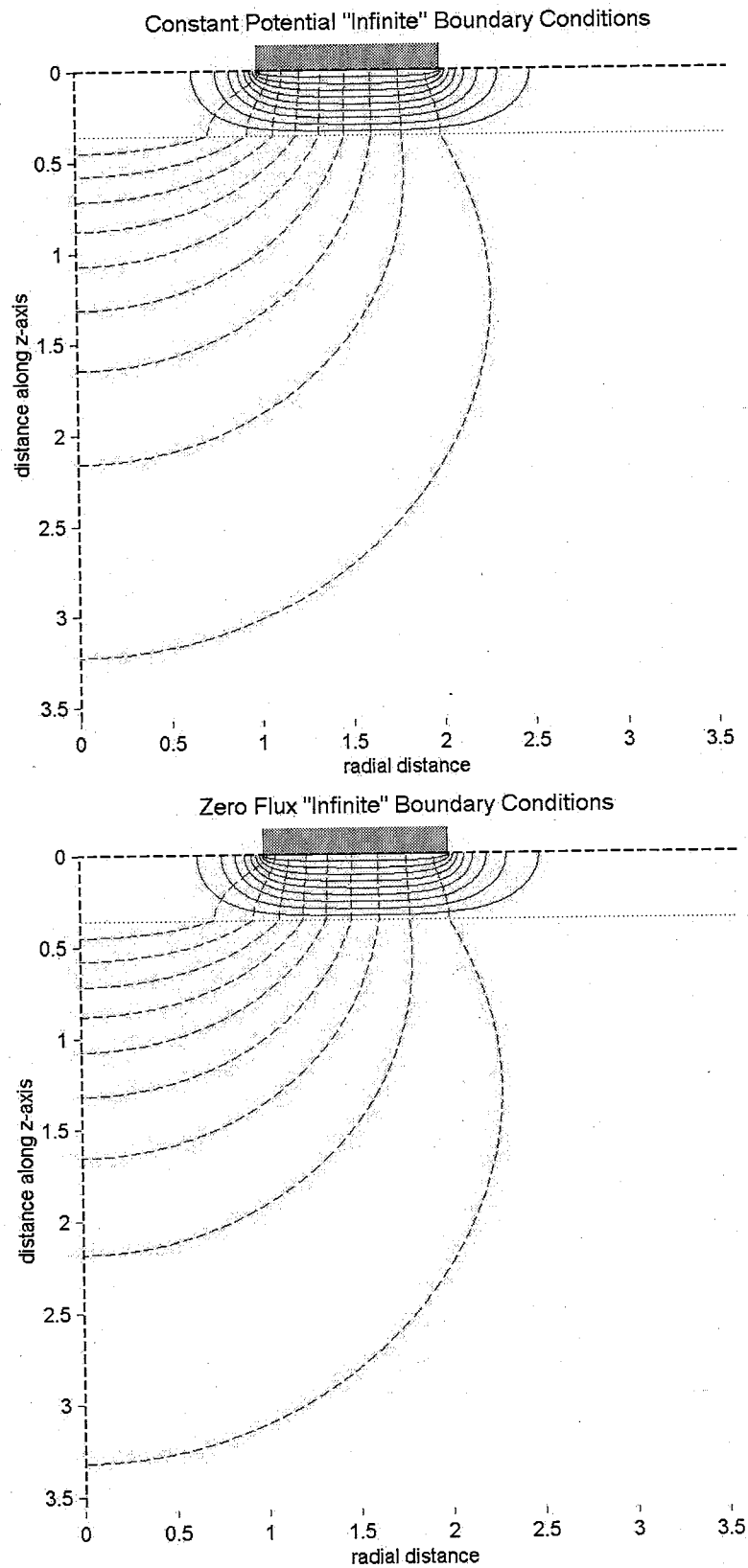
Figure 3.2 - Contours of dimensionless pseudo-potentials (dashed lines) and normalized stream functions (solid lines) for K_R=50, and D=0.357 (location indicated by dotted line). Both contour intervals are 0.10.

When the upper material is less permeable than the lower material ($K_R < 1$), the upper

material appears as a leaky seal that results in flow through a larger volume of rock.

In this case, it was important to insure that the boundary conditions did not

significantly effect simulation results. As K_R becomes increasingly smaller, the percent

difference in the geometric factors for simulations with the different boundary

conditions increases. For $K_R < 1$, the geometric factors in Table 3.1 are averages

from the geometric factors determined for the two different sets of boundary

conditions. These average values are less than 0.65 % different than the values

determined for either set of boundary conditions. Figure 3.3 presents the pseudo-

potential and streamlines for $K_R = 0.02$ and $D = 0.357$, for constant potential (Figure

3.3a) and zero flux (Figure 3.3b) boundary conditions. In the region near the tipseal,

no significant difference in the distribution of pseudo-potentials (dashed lines) or

streamlines (solid lines) is apparent.

Figure 3.4 presents the two-layer geometric factor values as a function of permeability

ratio for various dimensionless depths. For each dimensionless depth, the relationship

with permeability ratio is characterized by two asymptotes and a transition range. As

expected, as dimensionless depth increases, the two-layer geometric factor values

approach the single layer value, G_o, across the spectrum of permeability ratio values.

As the dimensionless depth decreases, the geometric factor within the transition region

is increasingly sensitive to the permeability ratio, and the asymptotic values

increasingly deviate from G_o.
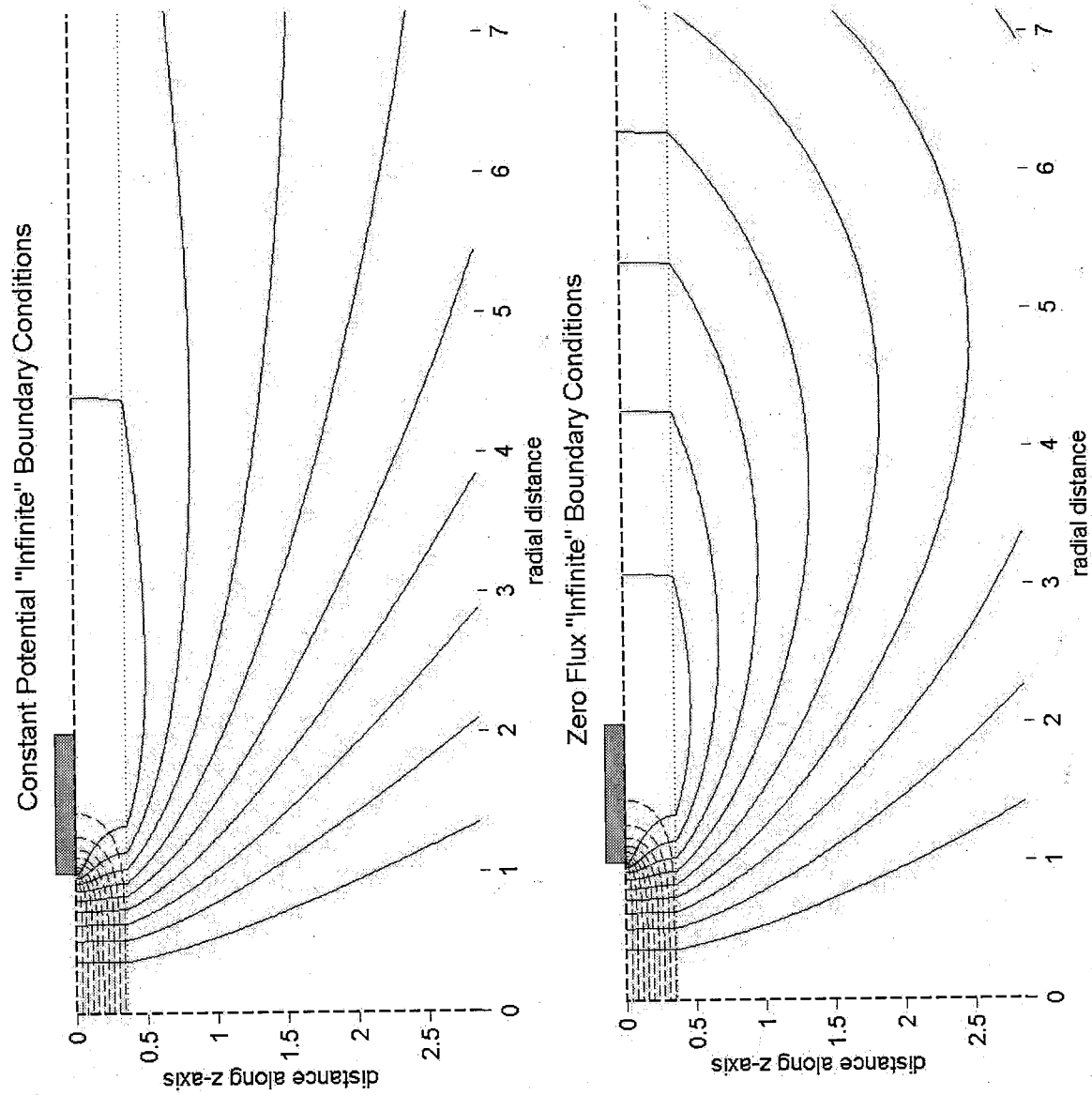
Figure 3.3 – Contours of dimensionless pseudo-potentials (dashed lines) and normalized stream functions (solid lines) for K_R=0.02, and D=0.357 (dotted line). Both contour intervals are 0.10.
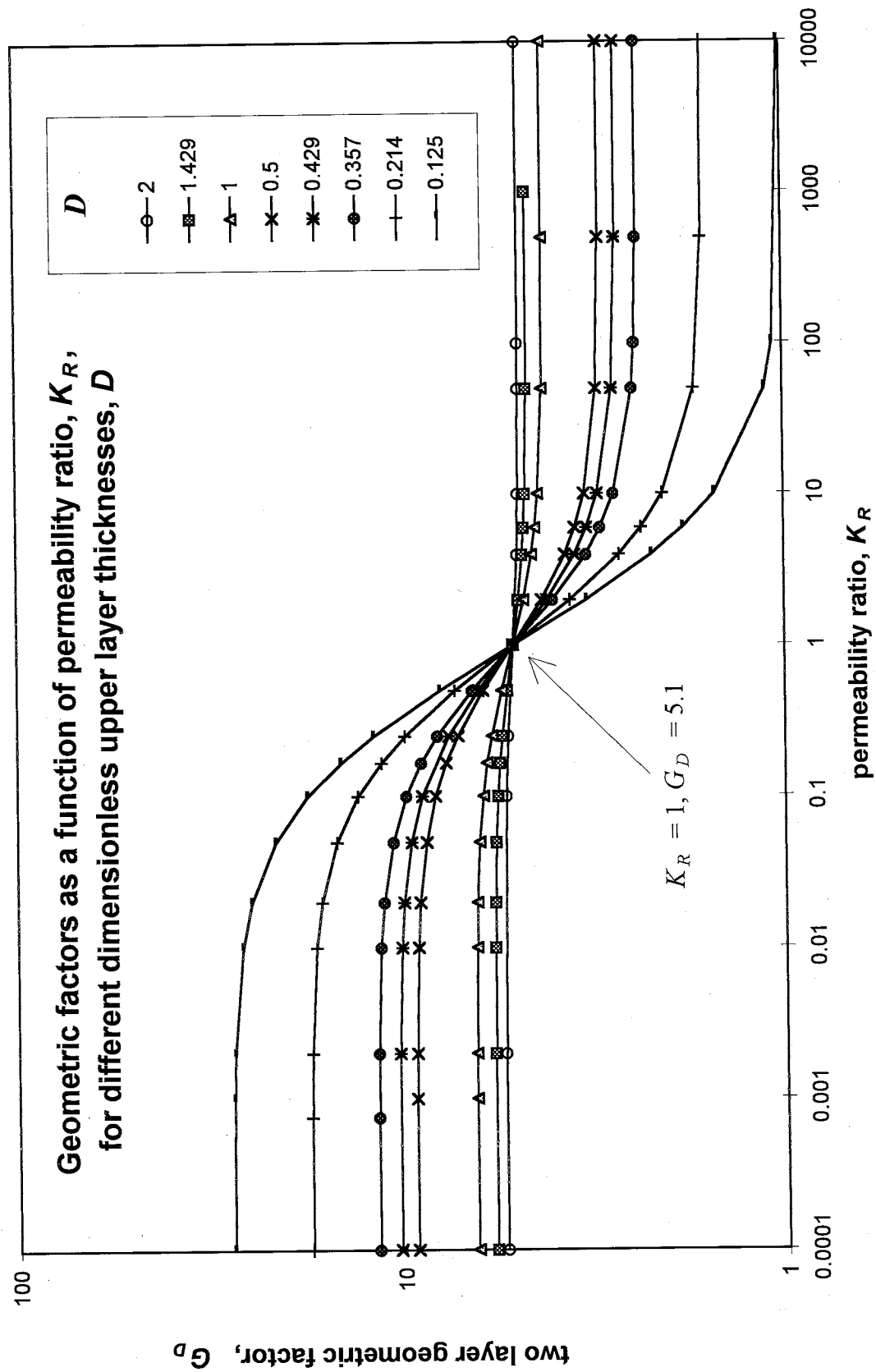
Figure 3.4 - Two-layer geometric factors, G_D, as a function of permeability ratio, K_R, for different dimensionless upper layer thickness, D. Data points are given by symbols and the lines represent regression curves.

In log-log space, the transition zone is centered at (or very near) the inflection point, $K_R = 1, G_D = G_o$ (determined from estimates of first derivatives), and does not appear to change as a function of dimensionless depth. Although the curves presented in Figure 3.4 appear to have symmetry about $K_R = 1, G_D = G_o$, at closer inspection, they become increasingly asymmetrical as dimensionless depth decreases.

Regression curves for the data in Figure 3.4 were obtained by identifying general equations that mimic the relationships observed, and then performing non-linear optimization to determine the fitting parameters. The optimization program utilized Newton-Raphson to drive the non-linear iteration and the method of least squares to solve the linear system of equations. For a particular dimensionless depth, (3.2) was found to best represent the behavior of the geometric factors. In this equation, A_{upper} and A_{lower} describe the upper and lower asymptotes, respectively, and are used to scale the equation. B_1 and B_2 are parameters that relate to the width and location of the transition zone.

$$(3.2) \qquad G_D(K_R) = \tfrac{1}{2}(A_{upper} - A_{lower})\mathit{erfc}(B_1 \log K_R + B_2) + A_{lower}$$

To insure that error was minimized for the entire range of permeability ratios, the optimization equation was formulated to find the least squares approximation that minimizes the percent error in G_D (3.3). This was found to provide a much better fit

for all data compared to minimizing the residual based on the numerator of (3.3) which resulted in considerable error for K_R greater than 1.

$$(3.3) \qquad \frac{G_D(\text{from data}) - G_D(\text{from equation 3.2})}{G_D(\text{from data})} .$$

The percent based optimization was performed in two ways: 1) by treating A_{upper}, A_{lower}, B_1 and B_2 as independent parameters, and 2) holding A_{upper} and A_{lower} constant (at the values generated from numerical data) and determining B_1 and B_2. Ultimately, fitting with all four parameters was utilized. It gave a slightly better overall fit to the numerically generated data, and the parameters yielded (Table 3.3) result in smooth curves when graphed versus the dimensionless depth (see Figure 3.5). This allows geometric factors to be graphically estimated for dimensionless depths for which numerical data was not directly obtained. To illustrate the accuracy of the regressions, Figure 3.5 was used to obtain the appropriate parameters for the dimensionless depth of interest, and the geometric factors were estimated. The estimates for all 133 data points were within 6.3%, and for dimensionless depths greater than or equal to 0.429, estimates of the geometric factors deviated less than 2% from the numerically generated values.
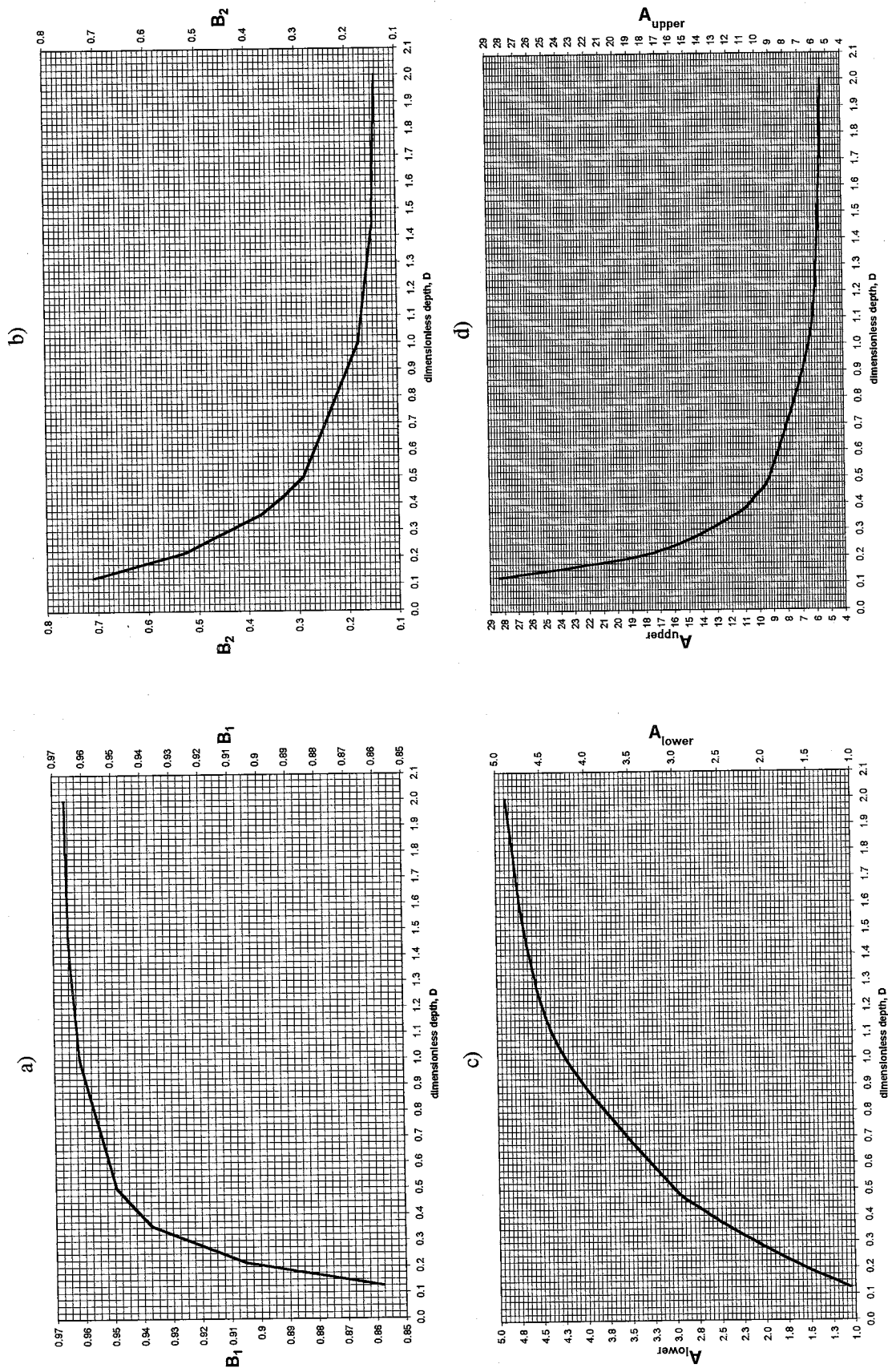
Figure 3.5 - Regression parameters B_1, B_2, A_{lower}, and A_{upper} as a function of dimensionless upper layer thickness, D.

	Dimensionless Depth, D							
	0.1250	0.2143	0.3571	0.4286	0.5000	1.0000	1.4286	2.0000
A_{upper}	28.34	17.53	11.68	10.25	9.25	6.44	5.75	5.40
A_{lower}	1.06	1.65	2.42	2.74	3.02	4.22	4.65	4.89
B_1	0.8576	0.9049	0.9372	0.9419	0.9491	0.9614	0.9648	0.9662
B_2	0.7092	0.5286	0.3755	0.3287	0.2894	0.1783	0.1496	0.1408

Table 3.3 - Parameters describing two-layer geometric factor regression curves (3.2).

The two-layer geometric factor depends on the permeability ratio between layers, making the two-layer form of the minipermeameter equation (3.1) non-linear. To address this, it was important to determine simple procedures that yield unique, accurate solutions and are easy to utilize. Two methods are proposed: a graphical procedure relying on either the data sets (Table 3.1) or regression curves (Figure 3.5), or a method that solves the regression equation and two-layer permeameter equation simultaneously through a non-linear optimization routine.

Important to both methods, is the manipulation of the governing equation to be written in terms of the unknown permeability ratio, K_R, and known second permeability value. For example, when the unknown permeability is the upper layer, the transformed minipermeameter equation can be re-written:

$$(3.4) \qquad K_R = \frac{1}{k_B} \frac{\dot{m}}{a\, G_D(b_d, D, K_R)\left[\Phi_i - \Phi_o\right]}$$

To invert the unknown permeability value, the user now has two equations, (3.2) and (3.4) and two unknowns, G_D and K_R. As illustrated in Figure 3.6, both equations are satisfied by only a single solution set. As the figure suggests, after determining the fitting parameters from Figure 3.5 or Table 3.3, the unknowns can be identified graphically. This may require graphing over increasingly smaller areas to precisely locate the intersection.

graphical estimate for measurement with mass flow of 148.9, difference in pseudo-potential of 1, and k_B=20
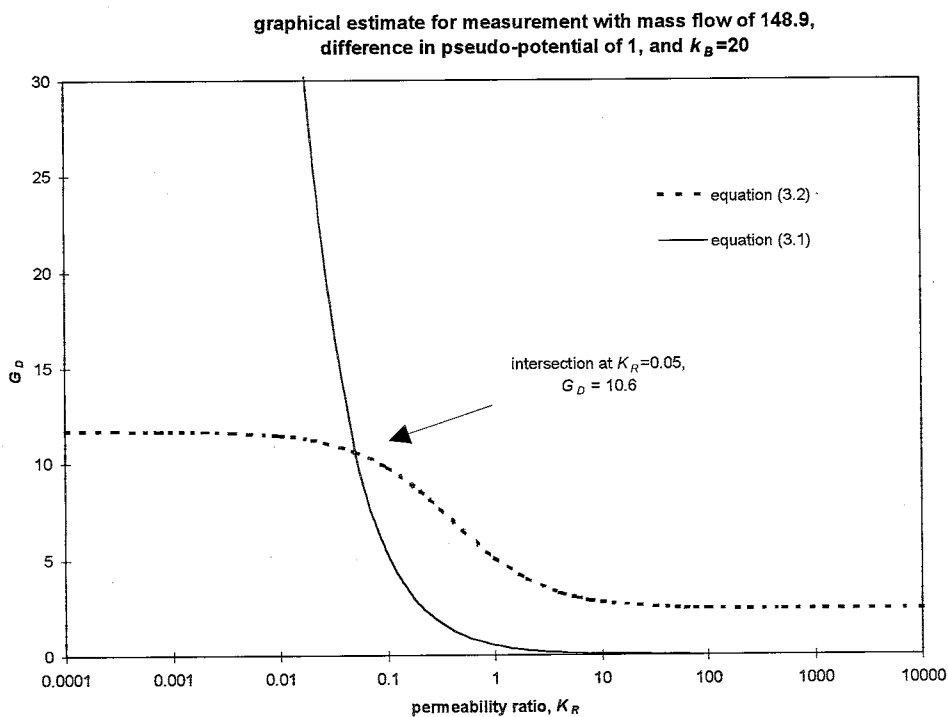
Figure 3.6 - Illustration of graphical technique used to determine the point (K_R, G_D) that satisfies both equations (3.1) and (3.2).

A slightly more complicated approach is to perform a non-linear search. Combining (3.2) and (3.4) yields a single non-linear equation (3.5), where G_D is the only unknown. To determine the value of G_D which satisfies (3.5), we implemented a simple non-linear search using Newton iteration to find the correct intersection point.

Using the single-layer geometric factor value, 5.10, as the initial guess, the search

quickly and precisely determines the two-layer geometric factor for our 133

"measurements", where the only error (other than experimental) is introduced by

determining the regression parameters (see previous paragraph).

$$(3.5) \qquad G_D = \tfrac{1}{2}(A_{upper} - A_{lower})erfc(B_1 \log_{10} \frac{C}{G_D} + B_2) + A_{lower}$$

$$\text{where} \quad C = \frac{\dot{m}}{k_B a \left[\Phi_i - \Phi_o \right]}$$

3.4 Conclusions

Geometric factors were determined for a two layer permeability system. These

geometric factors depend on the dimensionless thickness of the upper layer, D, and the

ratio of the upper layer permeability to the lower layer permeability, K_R. The two-

layer geometric factor, $G_D,(D,K_R)$ is utilized in place of the traditional single-layer

geometric factor, G_o, in the standard minipermeameter equation. These new

geometric factors can be used to determine the permeability of one layer when

independent measurements of the upper layer thickness of permeability of second layer

are available.

133 values of $G_D,(b_d = 2 ,D,K_R)$ were determined for flow into a semi-infinite sample.

Values for the geometric factor for $D > 2.0$ were not investigated since there is little

deviation (less than 6%) from the single layer geometric factor, G_o, regardless of the

permeability ratio. Values for geometric factors for $D < 0.125$ were also not

determined, since the geometric factor is becoming very sensitive to the permeability

ratio. For this case, it is recommended that a smaller tipseal be utilized.

For each value of D, a function describing G_D as a function of K_R was fit by

regression. This allows for approximating geometric factors for D and K_R

combinations not explicitly determined in the investigation. The regression curves

accurately reproduce all of the numerically generated geometric factors with less than

6.3 % error. Additionally, the regression curve equation may be utilized with the two-

layer minipermeameter equation (3.1) to determine the unknown layer permeability

either graphically or through a simple non-linear search.

Attempts were made to utilize the data from the laboratory experiments of Suboor

(1994) and Suboor and Heller (1995), to demonstrate practical implementation of the

two-layer geometric equation. They created a two-layer system composed of Berea

sandstone slices on top of high permeability glass beads. Based on the depth and ratio

of the material permeabilities, we used their data to estimate values for the two-layer

geometric factor, which all had $K_R < 1$.

Although the trends in the empirically estimated two-layer geometric factors matched

our numerically derived values, the empirical estimates were all considerably greater.

Based on the numerical investigation, I think the differences are easily explained: For

$K_R < 1$, the mass flow passed through the upper layer into the high permeability layer beneath. The lower permeability upper layer then acts as a barrier to flow which would normally escape through the adjacent sample surface, which in turn makes the magnitude of mass inflow very susceptible to the locations of the boundary conditions. This was observed and provided considerable issues in the numerical investigation (requiring domains as large as R_D=28.6,Z_D=34.3). If the side and bottom boundaries (of both the sandstone disc and beads) were not sealed, then the resulting mass flow would be increased causing the empirically estimated two layer geometric factors to be accordingly increased. Unfortunately, a description of the experimental boundary locations and boundary conditions were not available to verify this hypothesis.

In fault permeability studies, the upper layer is typically less permeable than the lower layer by several orders of magnitude. For $D \geq 0.125$, and $K_R \leq 0.01$, the two-layer geometric factor is approximated accurately by the upper asymptotic value (less than 6% error). For $K_R \leq 0.001$, the error is less than 0.58%. When the upper layer is more permeable than the lower layer, the asymptotic range is not approached as quickly. For $K_R \geq 10$, the percent difference from the asymptotic value is as much as 50% at $D = 0.125$. When the difference is at least three orders of magnitude ($K_R \geq 0.001$), the percent difference from the lower asymptotic value is less than 5%.

4. Conclusions and Recommendations

In the first investigation, *Determination of Spatial Weighting Functions Using Adjoint State Sensitivity Analysis*, the methodology for utilizing adjoint state sensitivity analysis to determine linear weighting functions is developed and implemented for the minipermeameter. It was shown that:

- Extension of a flow code to handle the adjoint state problem is relatively straightforward.

- The procedure offers a straightforward method to assess the relative importance of regions which contribute to the effective property that an instrument yields.

- For a homogeneous field, these spatial weighting function values represent the correct weights for any power law averaging process (arithmetic, geometric, harmonic, etc.).

Both volume averaged and point value weighting functions were determined and examined to give insight into the extent and relative importance of the regions sampled by the minipermeameter. These show:

- The region beneath the no-flow boundary of the tipseal has the largest influence on the effective permeability yielded by the instrument. In particular, the inner and outer edges of the region have the greatest impact.

- 95% of the region contributing to the effective permeability is contained within a right cylinder characterized by a dimensionless radius and length of 2.3, or a hemisphere characterized by a dimensionless radius of 2.5. 99% of the weighting function is contained in a cylinder with dimensionless lengths 3.71 or a hemisphere of 4.16.

- The region of interrogation determined from integrating the weighting functions are consistent with other investigations (experimental and numerical).

- The small scale detail provided agrees with what we would expect from intuitive observations of the stream potentials.

A very interesting correlation relating the spatial weighting functions to the geometric factor and pseudo-potential gradient was also discovered. Confidence in the proposed correlation is strengthened by the agreement of the units. Also, the appearance of the geometric factor is interesting, since it does not explicitly enter the calculations at any point.

As applied to the minipermeameter, the work should be expanded to determine the weighting functions for other tipseal ratios. Comparison of the weights for different ratios may lead to suggestions as to the appropriate tipseal ratio for particular investigations and optimal use recommendations. Additionally, further work needs to be done to establish whether the derived correlation holds up for other tipseal ratios, and whether the geometric factor for these ratios explicitly appears. Another possible option is examining the overall changes in the weighting functions when mildly heterogeneous fields are generated by stochastic methods.

Additionally, this technique should be applied to other instruments and tests, such as saturated flow toward a pumping well. These applications should offer further insight into the performance of these instruments/tests, and could be quickly addressed for 1D, 2D, and axisymmetric steady flow situations since the current finite element code could be used.

The second investigation, *Determination of Geometric Factors for a Layered Permeability System*, lays a foundation for the expansion of practical uses of the permeameter by introducing new geometric factors for layered permeability systems. The two-layer geometric factor, G_D,(D,K_R) is utilized in place of the traditional single-layer geometric factor, G_o, in the standard minipermeameter equation. For flow into a semi-infinite domain with a tipseal ratio (b_d) of 2, these new geometric factors:

- Can be used to determine the permeability of one layer when independent measurements are available for the upper layer thickness and the permeability of the second layer.

- Are functions of the dimensionless thickness of the upper layer, D, and the ratio of the upper layer permeability to the lower layer permeability, K_R.

- Are well described by the range of practical scenarios covered by the 133 values determined.

Values for the geometric factor for $D > 2.0$ were not investigated since there is little deviation (less than 6%) from the single layer geometric factor, G_o, regardless of the permeability ratio. Values for geometric factors for $D < 0.125$ were also not determined, since the geometric factor is becoming very sensitive to the permeability ratio. For this case, it is recommended that a smaller tipseal be utilized. Regression curves were determined to aid in inversion of field measurements, and so that intermediate values not numerically determined could be easily estimated. These curves:

- Allow for approximating geometric factors for D and K_R combinations not explicitly determined in the investigation.

- Accurately reproduce all of the numerically generated geometric factors with less than 6.3 % error.

- May be utilized with the two-layer minipermeameter equation to determine the unknown layer permeability either graphically or through a simple non-linear search.

- Are characterized by 4 fitting parameters that can be easily interpolated from a graph as a function of D.

In fault permeability studies, the upper layer is typically less permeable than the lower layer by several orders of magnitude. For $D \geq 0.125$ and $K_R \leq 0.01$, the two-layer geometric factor is approximated accurately by the upper asymptotic value (less than

6% error). For $K_R \leq 0.001$, the error is less than 0.58%. When the upper layer is more permeable than the lower layer, the asymptotic range is not approached as quickly. For $K_R \geq 10$, the percent difference from the asymptotic value is as much as 50% at $D = 0.125$. When the difference is at least three orders of magnitude ($K_R \geq 0.001$), the percent difference from the lower asymptotic value is less than 5%.

In field use, care should be taken to insure that the "infinite" boundaries are not approached. Simulation results showed that when the surface layer has lower permeability than the bottom layer, flow becomes trapped beneath the upper layer. In this case, the boundaries need be located at significantly larger distances so that they do not impact the rate of flow into the sample. Since the two layer permeameter equation is non-linear (due to the geometric factor's dependence on the permeability ratio), adjoint state sensitivity was not employed to determine the spatial weighting functions.

Current plans are to expand the geometric factors to address other tipseal sizes, beginning with a ratio of $b_d = 4$, and implement the two-layer geometric factors for investigating permeability alterations associated with faulting.

References

Antonellini, M.A., and A. Aydin, Effect of faulting on fluid flow in porous sandstones: petrophysical properties, *AAPG Bull.*, 78, 355-377, 1994.

Baveye, P., and G. Sposito, The operational significance of the continuum hypothesis in the theory of water movement through soils and aquifers, *Water Resour. Res.*, 20(5), 521-530, 1984.

Celia, M.A., and W.G. Gray, *Numerical methods for differential equations: fundamental concepts for scientific and engineering applications*, Prentice-Hall, Inc., Englewood Cliffs, New Jersey, 1992.

Chen, Z., Mathematical basis for permeability and porosity measurements by minipermeameter, MS Thesis, Petroleum Engineering Department, New Mexico Institute of Mining and Technology, Socorro, NM, 1992.

Cushman, J.H., On unifying the concepts of scale, instrumentation, and stochastics in the development of multiphase transport theory, *Water Resour. Res.*, 20(11), 1668-1678, 1984.

Davis, J.M., R.C. Lohmann, F.M. Phillips, J.L. Wilson, and D.W. Love, Architecture of the Sierra Ladrones Formation, Central New Mexico: depositional controls on the permeability correlation structure, *Geol. Soc. Am. Bull.*, 105(8), 998-1007, 1993.

Davis, J.M., J.L. Wilson, and F.M. Phillips, A portable air-minipermeameter for rapid in situ field measurements, *Ground Water*, 32(2), 258-266.

Desbarats, A.J., Spatial averaging of hydraulic conductivity in three-dimensional heterogeneous porous media, *Math. Geol.*, 24(3), 249-267, 1992.

Dreyer, T., A. Scheie, and O. Walderhaug, Minipermeameter-based study of permeability trends in channel and sand bodies, *AAPG Bull.*, 74(4), 359-374, 1990.

Dykstra, H. and Parsons, R.L., The prediction of oil recovery by waterflood, in Secondary recovery of oil in the United States, 2nd ed., *Am. Pet. Inst.*, New York, pp. 160-174, 1950.

Eijpe, R., and K.J. Weber, Mini-permeameters for consolidated rock and unconsolidated sand, *Am. Assoc. Petr. Geol. Bull.*, 55, 307-309, 1971.

Fowles, J. and Burley, S., Textural and permeability characteristics of faulted, high porosity sandstones, Marine and Petroleum Geology, 11(5), 608-623, 1994.

Goggin, D.J., R.L. Thrasher, and L.W. Lake, A theoretical and experimental analysis of minipermeameter response including gas slippage and high velocity flow effects, *In Situ*, 12(1-2), 79-116, 1988.

Huebner, K.H., and E.A. Thornton, *The finite element method for engineers.* John Wiley and Sons, New York, 1982.

Marle, C.-M., Ecoulements monophasiques em milieu poreux, *Rev. Inst. Fr. Petrol.*, 22, 1471-1509, 1967.

Matheron, G., *Les variables regionalisees et leur estimation*, Masson, Paris, 1965.

Sigda, J.M., L.B. Goodwin, P.S. Mozley, and J.L. Wilson, Permeability alteration in small-displacement faults in poorly lithified sediments: Rio Grande Rift, central New Mexico, Faults and Fluid Flow, eds. L. Goodwin and W. Haneberg, AGU Monograph, Washington D.C., American Geophysical Union, in press, 1999.

Suboor, M.A., The operating characteristics of the minipermeameter and its ability to investigate small scale permeability heterogeneity, MS Thesis, Dept. of Petroleum and Natural Gas Engineering, New Mexico Institute of Mining and Technology, Socorro, NM, 1994.

Suboor, M.A., and J.P. Heller, Minipermeameter characteristics critical to its use, *In Situ*, 19(3), 225-248, 1995.

Sun, N.-Z., *Inverse problems in groundwater modeling*, Kluwer Academic Publishers, Norwell, Massachusetts, 1994.

Tidwell, V.C., J.L. Wilson, and A.L. Gutjahr, Investigation of permeability upscaling: a multifaceted approach founded on laboratory and field experimentation, *Water Resour. Res.*, 35(1), 43-54, 1999.

Tidwell, V.C., J.L. Wilson, Laboratory method for investigating permeability upscaling, *Water Resour. Res.*, 33(7), 1607-1616, 1997.

Wang, F.W., M.P. Anderson, *Introduction to groundwater modeling: finite differences and finite element methods*, Academic Press, San Diego, California, 1982.

Yeh, T.-C.J., R. Srivastava, A. Guzman, and T. Harter, A numerical model for water and chemical transport in variably saturated porous media, *Ground Water*, 31(4), 634-644, 1993.

Srivastava, R., and T.-C.J. Yeh, A three-dimensional numerical model for water flow and transport of chemically reactive solute through porous media under variably saturated conditions, *Advances in Water Resources*, 15, 275-287, 1992.

APPENDIX A - Two-layer Simulations

D   0.125

"infinite" BC	d	a	D	k_B	k_T	K_R	$\Delta\Phi$	mass flux in	$G_D(D,K_R)$	% MBE
head	1.5	12	0.125	200	0.02	0.0001	0.2	1.34269	27.973	1.43E-02
flux	1.5	12	0.125	200	0.02	0.0001	0.2	1.33299	27.771	1.90E-03
head	1.5	12	0.125	200	0.2	0.001	0.2	13.34692	27.806	9.42E-03
flux	1.5	12	0.125	200	0.20	0.001	1	66.27181	27.613	2.84E-03
flux	1.5	12	0.125	40	0.08	0.002	1	26.34344	27.441	1.33E-03
head	1.5	12	0.125	40	0.08	0.002	1	26.51963	27.625	5.01E-03
head	1.5	12	0.125	10	0.1	0.01	1	31.54823	26.290	3.45E-03
flux	1.5	12	0.125	10	0.1	0.01	1	31.38992	26.158	2.58E-03
head	1.5	12	0.125	100	1	0.01	1	315.48229	26.290	8.44E-03
head	1.5	12	0.125	100	1	0.01	0.2	63.09643	26.290	3.96E-03
flux	1.5	12	0.125	100	1	0.01	1	313.89914	26.158	5.48E-03
head	1.5	12	0.125	50	1	0.02	1	298.18130	24.848	8.75E-03
flux	1.5	12	0.125	40	0.8	0.020	1	237.60525	24.751	3.49E-03
head	1.5	12	0.125	20	1	0.05	1	257.80260	21.484	1.05E-02
flux	1.5	12	0.125	20	1	0.05	1	257.11786	21.426	1.27E-02
head	1.5	12	0.125	10	1	0.1	1	212.43435	17.703	4.88E-03
head	1.5	12	0.125	6	1	0.1667	1	173.70056	14.475	6.62E-03
head	1.5	12	0.125	4	1	0.25	1	142.73332	11.894	8.31E-03
head	1.5	12	0.125	2	1	0.5	1	95.73487	7.978	4.77E-03
head	1.5	12	0.125	1	1	1	1	61.22468	5.102	2.28E-03
flux	1.5	12	0.125	1	1	1	1	61.15375	5.096	2.74E-03
head	1.5	12	0.125	1	2	2	1	78.48309	3.270	4.94E-03
head	1.5	12	0.125	1	4	4	1	106.04027	2.209	1.86E-03
head	1.5	12	0.125	1	6	6	1	131.58815	1.828	4.01E-03
head	1.5	12	0.125	1	10	10	1	181.24099	1.510	1.70E-03
head	1.5	12	0.125	0.1	5	50	0.2	13.36157	1.113	3.43E-04
head	1.5	12	0.125	1	50	50	1	668.07967	1.113	6.67E-04
head	1.5	12	0.125	0.1	10	100	1	127.49921	1.062	2.03E-04
flux	1.5	12	0.125	0.1	10	100	1	127.48331	1.062	1.92E-04
head	1.5	12	0.125	0.01	100	10000	0.2	242.79656	1.012	1.32E-04
flux	1.5	12	0.125	0.01	100	10000	0.2	242.79321	1.012	1.95E-04

D   0.214

"infinite" BC	d	a	D	k_B	k_T	K_R	$\Delta\Phi$	mass flux in	$G_D(D,K_R)$	% MBE
head	3	14	0.214	200	0.02	0.0001	2	9.833	17.559	7.5E-03
flux	3	14	0.214	200	0.02	0.0001	1	4.864	17.372	1.7E-03
head	3	14	0.214	200	0.15	0.00075	1	36.781	17.515	4.3E-03
flux	3	14	0.214	200	0.15	0.00075	1	36.395	17.331	1.4E-03
head	3	14	0.214	500	1	0.002	1	244.032	17.431	2.6E-03
flux	3	14	0.214	500	1	0.002	1	241.538	17.253	1.2E-03
head	3	14	0.214	50	0.5	0.01	1	118.458	16.923	2.4E-03
flux	3	14	0.214	50	0.5	0.01	1	117.420	16.774	1.4E-03
head	3	14	0.214	50	1	0.02	1	228.841	16.346	2.6E-03
flux	3	14	0.214	50	1	0.02	1	227.126	16.223	1.5E-03
head	3	14	0.214	20	1	0.05	1	208.552	14.897	2.7E-03
flux	3	14	0.214	20	1	0.05	1	207.418	14.816	1.9E-03
head	3	14	0.214	10	1	0.1	1	183.197	13.086	3.1E-03
head	3	14	0.214	6	1	0.1667	1	159.054	11.361	3.2E-03

"infinite" BC	d	a	D	k_B	k_T	K_R	$\Delta\Phi$	mass flux in	$G_D(D,K_R)$	% MBE
head	3	14	0.214	4	1	0.25	1	137.802	9.843	3.3E-03
head	3	14	0.214	2	1	0.5	1	101.606	7.258	2.1E-03
head	3	14	0.214	1	1	1	1	71.450	5.104	2.0E-03
flux	3	14	0.214	1	1	1	1	71.317	5.094	1.9E-03
head	3	14	0.214	1	2	2	1	100.847	3.602	1.5E-03
head	3	14	0.214	1	4	4	1	150.254	2.683	1.4E-03
head	3	14	0.214	1	6	6	1	196.916	2.344	1.2E-03
head	3	14	0.214	1	10	10	1	288.306	2.059	9.5E-04
head	3	14	0.214	1	50	50	1	1189.608	1.699	4.1E-04
head	3	14	0.214	1	500	500	1	11308.330	1.615	2.8E-04
head	3	14	0.214	0.05	500	10000	1	11246.048	1.607	2.1E-04
flux	3	14	0.214	0.05	500	10000	1	11245.830	1.607	2.3E-04

D	0.357

"infinite" BC	d	a	D	k_B	k_T	K_R	$\Delta\Phi$	mass flux in	$G_D(D,K_R)$	% MBE
head	5	14	0.357	200	0.02	0.0001	3	9.8867	11.770	1.0E-02
flux	5	14	0.357	200	0.02	0.0001	1	3.2569	11.632	3.0E-03
head	5	14	0.357	200	0.15	0.00075	1	24.6799	11.752	4.2E-03
flux	5	14	0.357	200	0.15	0.00075	1	24.3931	11.616	1.8E-03
head	5	14	0.357	500	1	0.002	1	164.0637	11.719	5.2E-03
flux	5	14	0.357	500	1	0.002	1	162.1885	11.585	2.4E-03
head	5	14	0.357	500	1	0.002	0.3	49.2191	11.719	4.2E-03
head	2.5	7	0.357	500	1	0.002	1	82.04092	11.720	4.5E-03
head	5	14	0.357	100	1	0.01	1	161.1737	11.512	5.2E-03
flux	5	14	0.357	100	1	0.01	1	159.5093	11.394	3.0E-03
head	5	14	0.357	100	1	0.01	0.3	48.3520	11.512	4.1E-03
head	5	14	0.357	50	1	0.02	1	157.7994	11.271	4.3E-03
flux	5	14	0.357	50	1	0.02	1	156.3424	11.167	2.8E-03
head	5	14	0.357	50	1	0.02	0.3	47.3398	11.271	4.4E-03
head	2.5	7	0.357	50	1	0.02	1	78.85787	11.265	3.8E-03
head	5	14	0.357	20	1	0.05	1	148.9201	10.637	4.7E-03
flux	5	14	0.357	20	1	0.05	1	147.8629	10.562	3.1E-03
head	5	14	0.357	10	1	0.1	1	137.0358	9.788	4.5E-03
head	5	14	0.357	10	1	0.1	0.3	41.1109	9.788	4.3E-03
head	2.5	7	0.357	10	1	0.1	1	68.47346	9.782	3.0E-03
head	5	14	0.357	6	1	0.1667	1	124.8448	8.917	2.8E-03
head	5	14	0.357	6	1	0.1667	0.3	37.4534	8.917	4.0E-03
head	2.5	7	0.357	6	1	0.1667	1	62.3893	8.913	2.4E-03
head	5	14	0.357	4	1	0.25	1	113.3191	8.094	3.0E-03
head	5	14	0.357	4	1	0.25	0.3	33.9958	8.094	3.5E-03
head	2.5	7	0.357	4	1	0.25	1	56.63518	8.091	2.4E-03
head	5	14	0.357	2	1	0.5	1	91.7004	6.550	3.0E-03
head	5	14	0.357	2	1	0.5	0.3	27.5103	6.550	3.7E-03
head	2.5	7	0.357	2	1	0.5	1	45.83714	6.548	2.3E-03
head	5	14	0.357	1	1	1	1	71.4429	5.103	2.1E-03
flux	5	14	0.357	1	1	1	1	71.3104	5.094	1.5E-03
head	5	14	0.357	1	1	1	0.3	21.4329	5.103	3.0E-03
head	2.5	7	0.357	1	1	1	1	35.71557	5.102	1.4E-03
flux	2.5	7	0.357	1	1	1	1	35.7074	5.101	1.3E-03
head	5	14	0.357	1	2	2	1	111.8485	3.995	1.4E-03
head	5	14	0.357	2	4	2	1	223.6984	3.995	1.4E-03
head	5	14	0.357	4	8	2	1	447.3904	3.995	1.4E-03
head	5	14	0.357	1	2	2	0.3	33.5541	3.995	1.5E-03
"infinite" BC	d	a	D	k_B	k_T	K_R	$\Delta\Phi$	mass flux in	$G_D(D,K_R)$	% MBE

								mass flux in		% MBE
head	2.5	7	0.357	1	2	2	1	55.92099	3.994	1.1E-03
head	5	14	0.357	1	4	4	1	183.2936	3.273	1.1E-03
head	5	14	0.357	20	80	4	1	3665.8994	3.273	9.4E-04
head	5	14	0.357	2	8	4	1	366.5852	3.273	1.0E-03
head	5	14	0.357	2	8	4	0.3	109.9767	3.273	1.1E-03
head	5	14	0.357	1	4	4	0.3	54.9881	3.273	8.8E-04
head	2.5	7	0.357	1	4	4	1	91.65074	3.273	9.1E-04
head	5	14	0.357	1	6	6	1	251.8739	2.998	7.6E-04
head	5	14	0.357	1	6	6	0.3	75.5607	2.998	8.2E-04
head	2.5	7	0.357	1	6	6	1	125.9476	2.999	6.3E-04
head	2.5	7	0.357	1	6	6	0.5	62.97357	2.999	6.1E-04
head	5	14	0.357	1	10	10	1	386.9757	2.764	6.5E-04
head	5	14	0.357	1	10	10	0.3	116.0917	2.764	7.0E-04
head	5	14	0.357	1	10	10	0.2	77.3946	2.764	
head	5	14	0.357	1	10	10	0.5	193.4879	2.764	7.4E-04
head	5	14	0.357	1	10	10	0.7	270.8799	2.764	8.6E-04
head	5	14	0.357	1	10	10	1.5	580.4562	2.764	7.8E-04
head	5	14	0.357	1	10	10	5	1934.8723	2.764	6.3E-04
head	2.5	7	0.357	1	10	10	1	193.51377	2.764	4.7E-04
head	5	14	0.357	1	50	50	1	1724.5123	2.464	5.0E-04
flux	5	14	0.357	1	50	50	1	1724.3758	2.463	4.0E-04
head	5	14	0.357	1	50	50	0.3	517.3537	2.464	6.1E-04
head	2.5	7	0.357	1	50	50	1	862.43569	2.464	2.1E-04
head	5	14	0.357	1	100	100	1	3394.2101	2.424	4.2E-04
flux	5	14	0.357	1	100	100	1	3394.0395	2.424	5.0E-04
head	5	14	0.357	1	100	100	2	6788.5196	2.424	4.7E-04
head	5	14	0.357	1	100	100	3	10182.4847	2.424	4.7E-04
head	5	14	0.357	1	100	100	5	16970.9204	2.424	4.3E-04
head	5	14	0.357	1	100	100	0.3	1018.2586	2.424	4.6E-04
head	5	14	0.357	1	500	500	1	16749.7596	2.393	4.7E-04
flux	5	14	0.357	1	500	500	1	16749.7582	2.393	5.4E-04
head	5	14	0.357	1	500	500	0.3	5024.9343	2.393	5.4E-04
flux	5	14	0.357	1	500	500	3	50249.2628	2.393	4.4E-04
flux	5	14	0.357	1	500	500	5	83749.2864	2.393	5.9E-04
head	2.5	7	0.357	1	500	500	1	8376.94347	2.393	1.5E-04
head	5	14	0.357	0.05	500	10000	1	16697.1880	2.385	4.9E-04

D 0.429

"infinite" BC	d	a	D	k_B	k_T	K_R	$\Delta\Phi$	mass flux in	$G_D(D,K_R)$	% MBE
head	6	14	0.429	200	0.02	0.0001	1	2.89514	10.340	9.67E-03
flux	6	14	0.429	200	0.02	0.0001	1	2.85992	10.214	3.19E-03
head	6	14	0.429	500	1	0.002	1	144.24075	10.303	6.11E-03
flux	6	14	0.429	500	1	0.002	1	142.52656	10.180	3.00E-03
head	6	14	0.429	100	1	0.01	1	142.14458	10.153	5.30E-03
flux	6	14	0.429	100	1	0.01	1	140.59776	10.043	3.41E-03
head	6	14	0.429	50	1	0.02	1	139.67941	9.977	5.22E-03
flux	6	14	0.429	50	1	0.02	1	138.30194	9.879	3.61E-03
head	6	14	0.429	20	1	0.05	1	133.11223	9.508	5.17E-03
flux	6	14	0.429	20	1	0.05	1	132.07962	9.434	3.69E-03
head	6	14	0.429	10	1	0.1	1	124.16301	8.869	2.97E-03
head	6	14	0.429	4	1	0.25	1	105.77717	7.556	3.53E-03
head	6	14	0.429	2	1	0.5	1	88.36849	6.312	3.05E-03
head	6	14	0.429	1	1	1	1	71.44161	5.103	2.13E-03
"infinite" BC	d	a	D	k_B	k_T	K_R	$\Delta\Phi$	mass flux in	$G_D(D,K_R)$	% MBE
flux	6	14	0.429	1	1	1	1	71.30872	5.093	1.92E-03
head	6	14	0.429	1	2	2	1	116.09080	4.146	1.52E-03
head	6	14	0.429	1	4	4	1	196.48330	3.509	1.21E-03

"infinite" BC	d	a	D	k_B	k_T	K_R	$\Delta\Phi$	mass flux in	$G_D(D, K_R)$	% MBE
head	6	14	0.429	1	6	6	1	274.08735	3.263	1.05E-03
head	6	14	0.429	1	10	10	1	427.26769	3.052	6.43E-04
head	6	14	0.429	1	50	50	1	1945.68664	2.780	4.45E-04
head	6	14	0.429	1	500	500	1	19005.90748	2.715	5.14E-04
head	6	14	0.429	0.02	200	10000	1	7583.07842	2.708	5.80E-04
flux	6	14	0.429	0.02	200	10000	1	7582.95942	2.708	5.15E-04

D 0.500

"infinite" BC	d	a	D	k_B	k_T	K_R	$\Delta\Phi$	mass flux in	$G_D(D, K_R)$	% MBE
head	7	14	0.50	200	0.02	0.0001	1	2.6120	9.329	1.1E-02
flux	7	14	0.50	200	0.02	0.0001	1	2.5794	9.212	2.9E-03
head	7	14	0.50	100	0.1	0.001	1	13.0414	9.315	9.2E-03
flux	7	14	0.50	100	0.1	0.001	1	12.8803	9.200	2.5E-03
head	7	14	0.50	500	1	0.002	1	130.2094	9.301	5.0E-03
head	7	14	0.50	50	0.1	0.002	0.2	2.6042	9.301	1.1E-02
flux	7	14	0.50	50	0.1	0.002	1	12.8618	9.187	2.3E-03
head	7	14	0.50	100	1	0.01	1	128.6156	9.187	4.5E-03
flux	7	14	0.50	100	1	0.01	1	127.1608	9.083	2.1E-03
head	7	14	0.50	50	1	0.02	1	126.7305	9.052	3.8E-03
head	7	14	0.50	50	1	0.02	0.2	25.3461	9.052	9.5E-03
flux	7	14	0.50	50	1	0.02	1	125.4190	8.959	2.1E-03
head	7	14	0.50	20	1	0.05	1	121.6652	8.690	3.8E-03
flux	7	14	0.50	20	1	0.05	1	120.6566	8.618	2.2E-03
head	7	14	0.50	10	1	0.1	1	114.6715	8.191	3.5E-03
head	7	14	0.50	6	1	0.1667	1	107.2521	7.661	3.8E-03
head	7	14	0.50	4	1	0.25	1	100.0008	7.143	3.9E-03
head	7	14	0.50	2	1	0.5	1	85.7202	6.123	3.5E-03
head	7	14	0.50	1	1	1	1	71.4393	5.103	2.3E-03
flux	7	14	0.50	1	1	1	1	71.3074	5.093	1.9E-03
head	7	14	0.50	1	2	2	1	119.6864	4.275	1.5E-03
head	7	14	0.50	1	4	4	1	207.8697	3.712	1.2E-03
head	7	14	0.50	1	6	6	1	293.3907	3.493	1.1E-03
head	7	14	0.50	1	10	10	1	462.4855	3.303	9.0E-04
head	7	14	0.50	1	50	50	1	2140.3649	3.058	8.6E-04
head	7	14	0.50	1	500	500	1	20995.2037	2.999	7.3E-04
head	7	14	0.50	0.02	200	10000	1	8380.6726	2.993	7.3E-04
flux	7	14	0.50	0.02	200	10000	1	8380.6451	2.993	7.2E-04

D 1.000

"infinite" BC	d	a	D	k_B	k_T	K_R	$\Delta\Phi$	mass flux in	$G_D(D, K_R)$	% MBE
head	7	7	1.0	200	0.02	0.0001	1	0.90485	6.463	1.01E-02
flux	7	7	1.0	200	0.02	0.0001	1	0.90211	6.444	4.76E-03
head	7	7	1.0	200	0.2	0.001	1	9.04332	6.460	9.69E-03
flux	7	7	1.0	200	0.2	0.001	1	9.01634	6.440	3.46E-03
head	7	7	1.0	500	1	0.002	1	45.18831	6.455	4.60E-03
flux	7	7	1.0	500	1	0.002	1	45.05509	6.436	3.75E-03
head	7	7	1.0	100	1	0.01	1	44.96756	6.424	6.10E-03
flux	7	7	1.0	100	1	0.01	1	44.84697	6.407	4.53E-03

"infinite" BC	d	a	D	k_B	k_T	K_R	$\Delta\Phi$	mass flux in	$G_D(D, K_R)$	% MBE
head	7	7	1.0	50	1	0.02	1	44.70435	6.386	5.91E-03
flux	7	7	1.0	50	1	0.02	1	44.59716	6.371	4.74E-03
head	7	7	1.0	20	1	0.05	1	43.98486	6.284	5.89E-03
flux	7	7	1.0	20	1	0.05	1	43.90546	6.272	4.96E-03
head	7	7	1.0	10	1	0.1	1	42.96173	6.137	5.73E-03

BC	d	a	D	k_B	k_T	K_R	$\Delta\Phi$	mass flux in	$G_D(D,K_R)$	% MBE
head	7	7	1.0	6	1	0.1667	1	41.83653	5.977	5.39E-03
head	7	7	1.0	4	1	0.25	1	40.69446	5.813	5.01E-03
head	7	7	1.0	2	1	0.5	1	38.30908	5.473	4.02E-03
head	7	7	1.0	1	1	1	1	35.72000	5.103	2.95E-03
flux	7	7	1.0	1	1	1	1	35.70550	5.101	2.87E-03
head	7	7	1.0	1	2	2	1	66.84515	4.775	2.26E-03
head	7	7	1.0	1	4	4	1	127.03040	4.537	1.67E-03
head	7	7	1.0	1	6	6	1	186.49636	4.440	1.67E-03
head	7	7	1.0	1	10	10	1	304.86768	4.355	1.66E-03
head	7	7	1.0	1	50	50	1	1484.78851	4.242	1.13E-03
head	7	7	1.0	1	500	500	1	14752.22969	4.215	1.23E-03
flux	7	7	1.0	1	500	500	1	14752.25402	4.215	1.05E-03
head	7	7	1.0	0.02	200	10000	1	5896.78348	4.212	1.05E-03

D   1.429

"infinite" BC	d	a	D	k_B	k_T	K_R	$\Delta\Phi$	mass flux in	$G_D(D,K_R)$	% MBE
head	10	7	1.4286	100	0.01	0.0001	1	0.40329	5.761	8.22E-03
flux	10	7	1.4286	100	0.01	0.0001	1	0.40223	5.746	3.19E-03
head	10	7	1.4286	40	0.08	0.002	0.5	1.61219	5.758	8.56E-03
flux	10	7	1.4286	40	0.08	0.002	1	3.21604	5.743	2.25E-03
head	10	7	1.4286	25	0.25	0.01	1	10.05089	5.743	1.10E-02
flux	10	7	1.4286	25	0.25	0.01	1	10.02668	5.730	3.79E-03
head	10	7	1.4286	25	0.5	0.02	1	20.04107	5.726	1.08E-02
flux	10	7	1.4286	25	0.5	0.02	1	19.99667	5.713	4.45E-03
head	10	7	1.4286	10	0.5	0.05	1	19.87346	5.678	8.08E-03
head	10	7	1.4286	10	1	0.1	0.1	3.92639	5.609	4.72E-03
head	10	7	1.4286	6	1	0.1667	1	38.72654	5.532	5.75E-03
head	10	7	1.4286	4	1	0.25	1	38.17588	5.454	5.41E-03
head	10	7	1.4286	2	1	0.5	1	37.00979	5.287	5.13E-03
head	10	7	1.4286	1	1	1	1	35.71685	5.102	4.28E-03
flux	10	7	1.4286	1	1	1	1	35.70872	5.101	4.01E-03
head	10	7	1.4286	1	2	2	1	69.10665	4.936	3.52E-03
head	10	7	1.4286	1	4	4	1	134.77481	4.813	3.42E-03
head	10	7	1.4286	1	6	6	1	200.04811	4.763	1.63E-03
head	10	7	1.4286	1	10	10	1	330.29066	4.718	2.30E-03
head	10	7	1.4286	0.2	10	50	0.2	65.22295	4.659	3.53E-03
head	10	7	1.4286	0.02	20	1000	0.4	260.03403	4.643	3.61E-03
flux	10	7	1.4286	0.02	20	1000	0.4	260.03291	4.643	3.25E-03

D   2.000

"infinite" BC	d	a	D	k_B	k_T	K_R	$\Delta\Phi$	mass flux in	$G_D(D,K_R)$	% MBE
head	14	7	2.0	100	0.01	0.0001	1	0.37830	5.404	5.10E-03
flux	14	7	2.0	100	0.01	0.0001	1	0.37785	5.398	3.65E-03
head	14	7	2.0	40	0.08	0.002	1	3.02553	5.403	5.30E-03
flux	14	7	2.0	40	0.08	0.002	1	3.02197	5.396	1.63E-03
head	14	7	2.0	10	1	0.1	1	37.35133	5.336	4.29E-03

"infinite" BC	d	a	D	k_B	k_T	K_R	$\Delta\Phi$	mass flux in	$G_D(D,K_R)$	% MBE
flux	14	7	2.0	10	1	0.1	1	37.32884	5.333	6.46E-03
head	14	7	2.0	4	1	0.25	1	36.85603	5.265	3.20E-03
head	14	7	2.0	1	1	1	1	35.71938	5.103	2.27E-03
flux	14	7	2.0	1	1	1	1	35.71573	5.102	2.31E-03
head	14	7	2.0	1	4	4	1	139.0723	4.967	2.51E-03
head	14	7	2.0	1	10	10	1	344.52071	4.922	1.68E-03
head	14	7	2.0	1	50	50	1	1712.66141	4.893	1.06E-03

head	14	7	2.0	1	100	100	1	3422.66956	4.890	1.03E-03
head	14	7	2.0	0.01	100	10000	1	3419.97611	4.886	1.12E-03
flux	14	7	2.0	0.01	100	10000	1	3419.97611	4.886	1.12E-03